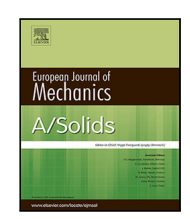
ELSEVIER

Contents lists available at ScienceDirect

European Journal of Mechanics / A Solids

journal homepage: www.elsevier.com/locate/ejmsol



Full length article

Size effects in 3D-printed polymeric lattices under three-point bending: Manufacturing, testing, and modelling

Wanderson F. dos Santos ^a, Alina S.L. Rodrigues ^b, Igor A. Rodrigues Lopes ^c, Francisco M. Andrade Pires ^d, Sergio P.B. Proença ^a, Zilda C. Silveira ^b

- a Departamento de Engenharia de Estruturas, Escola de Engenharia de São Carlos, Universidade de São Paulo, Av. Trabalhador São-Carlense, 13566-590 São Carlos. Brazil
- b Departamento de Engenharia Mecânica, Escola de Engenharia de São Carlos, Universidade de São Paulo, Av. Trabalhador São-Carlense, 13566-590 São Carlos. Brazil
- ^c INEGI-LAETA, Instituto de Ciência e Inovação em Engenharia Mecânica e Engenharia Industrial, Universidade do Porto, Rua Dr. Roberto Frias, 400, 4200-465, Porto Portugal
- d INEGI-LAETA, Faculdade de Engenharia, Universidade do Porto, Rua Dr. Roberto Frias, 4200-465 Porto, Portugal

ARTICLE INFO

Keywords: Lattice structures Size effects FDM-based manufacturing Three-point bending DNS finite element models Multi-scale modelling

ABSTRACT

Architected lattice structures often exhibit pronounced size effects that challenge conventional modelling strategies. This contribution presents a combined experimental and numerical investigation of size effects in 3D-printed lattice beams under three-point bending. Specimens with triangular and square unit cells, manufactured using affordable Fused Deposition Modelling (FDM) with polyethylene terephthalate glycol (PETG), are tested at different lattice refinements while maintaining constant overall dimensions and solid volume fraction. The experiments reveal clear size-dependent behaviour in terms of stiffness, strength, and failure modes. To model these effects, three numerical strategies are employed: Direct Numerical Simulations (DNS), and multi-scale approaches based on first- and second-order computational homogenisation (FE²).DNS provides accurate predictions but is computationally expensive for fine lattices. Second-order FE² captures size effects more efficiently, particularly when micro-scale periodic boundary conditions are applied, although it may overestimate responses for coarser lattices. This work critically assesses the accuracy and applicability of each modelling approach, providing valuable insight into the design and simulation of architected structures where scale-dependent behaviour is significant.

1. Introduction

Architected structures are characterised by their morphology, which consists of a pattern of repeated unit cells with specific morphology (a lattice structure). The size of the unit cell may range several length scales (e.g., meso-scale, micro-scale and/or nano-scale architecture) and the combination of the underlying materials properties of the solid phase with its geometric features and the interaction with the global loading conditions dictate the mechanical behaviour of the architected structure. Therefore, it is possible to tailor the mechanical behaviour of architected metamaterials, enabling the design of innovative lattice structures to achieve exceptional structural efficiency and unprecedented mechanical properties, beyond those of conventional natural materials (Jiao et al., 2023). For instance, cellular and lattice materials offer high strength-to-weight ratio, large deformability, specific energy

absorption, vibration control, thermal management and sound absorption (Fleck et al., 2010; Schaedler and Carter, 2016; Andersen et al., 2021; Benedetti et al., 2021; Li et al., 2021; Qi et al., 2021; Zhang et al., 2022; Yavas et al., 2022; Wang et al., 2022; Yin et al., 2023; Wang et al., 2024). Furthermore, these classes of material can be designed to attain more lightweight and sustainable structural solutions, reducing material usage and energy consumption (Nazir et al., 2019; Wu et al., 2023a), with potential applications in the civil engineering (Chica and Alzate, 2019; Tiwari et al., 2024), automotive (Tay et al., 2014; Tilley et al., 2024), and aerospace (Ferro et al., 2018; Opgenoord and Willcox, 2021; Smeets et al., 2021) industries, as well as in biomedical applications (Mahmoud and Elbestawi, 2017; Ataollahi, 2023). Nevertheless, there are still obstacles to overcome in the design and manufacturing of architected materials due to possibly intricate geometries and resulting complex mechanical behaviour.

E-mail address: ilopes@inegi.up.pt (I.A. Rodrigues Lopes).

^{*} Corresponding author.

Regarding their manufacturing, Spadaccini (2019) highlights challenging aspects related to the morphological complexity of many threedimensional structures, multiple length scales, the possibility of incorporating different material constituents and the overall manufacturing throughput. The above-mentioned characteristics reveal limitations of conventional manufacturing technologies for fabricating more advanced architected structures, leading to highly complex and costly structure-based designs (Nazir et al., 2019). Nevertheless, new developments in the context of additive manufacturing (AM), also referred to as 3D printing, have opened up new possibilities for the development and design of sophisticated architected structures. Thus, the advancement of 3D printing technologies enables more feasible tailored structures with multi-functional properties provided by the precise control of the microstructural unit cell (Benedetti et al., 2021; Uribe-Lam et al., 2021; Yang et al., 2024; Bhat et al., 2024). It is worth noting that economically efficient structures with optimal shapes have been designed by combining topology optimisation strategies with additive manufacturing (Nazir et al., 2019; Plocher and Panesar, 2019; Pan et al., 2020; Kladovasilakis et al., 2023).

A wide variety of materials, encompassing metals, polymers, ceramics, and polymer-composite materials, have been employed to fabricate architected structures through additive manufacturing (Benedetti et al., 2021). Depending on the application and feedstock, various additive manufacturing techniques can be used to fabricate architected structures, including Fused Filament Fabrication (FFF) or Fused Deposition Modeling (FDM), Stereolithography (SLA), Material Jetting, Binder Jetting, Selective Laser Sintering (SLS), Selective Laser Melting (SLM), and Directed Energy Deposition (DED) (Kladovasilakis et al., 2022). In particular, FDM is an attractive manufacturing process for customised structures made from polymeric architected materials (Cuan-Urquizo and Silva, 2023), combining ease of manufacturing and cost efficiency to produce lightweight components with suitable mechanical performance; hence, it is the technique adopted in the present contribution. This 3D printing process is based on building a physical object layer by layer, where a thermoplastic material is melted and extruded through a heated nozzle. In this case, polymeric materials such as PETG, polylactic acid (PLA), acrylonitrile butadiene styrene (ABS), and thermoplastic polyurethane (TPU) can be used as feedstock, for instance.

It is also worth noting that architected structures, particularly those with thin-walled elements, exhibit complex mechanical behaviour comprising strain localisation mechanisms and stress concentrations, as well as boundary layer phenomena, size effects and deformation mode coupling (Iltchev et al., 2015; Kladovasilakis et al., 2022; dell'Isola et al., 2019; Korshunova et al., 2021; Pham and Hütter, 2021; dos Santos et al., 2024). Therefore, standard macroscopic simulations with conventional homogenised constitutive laws may not capture their mechanical response accurately. A possible approach to overcome that issue involves DNS models, consisting of detailed single-scale simulations where the solid part at the micro-architecture level is explicitly discretised into fine elements. Although DNS finite element models show good agreement with the experimental results, the numerical simulations can be computationally expensive and even prohibitive for complete modelling of complex architected structures in industrial applications (Tekoglu and Onck, 2005; Iltchev et al., 2015). This is particularly critical considering that optimal unit cells may be designed by combining topology optimisation strategies based on iterative simulations with additive manufacturing (Plocher and Panesar, 2019; Nazir et al., 2019; Pan et al., 2020; Kladovasilakis et al., 2023).

It has been shown that multi-scale models based on computational homogenisation (FE²), where both the macro-scale and the micro-scale domains are with distinct but coupled finite element problems, may significantly reduce the computational effort of the simulation of architected metamaterials (dos Santos et al., 2023), compared to DNS approaches. The macroscopic structure is assumed to be a homogenised continuum with effective constitutive behaviour derived from average-based homogenisation theory applied to the microscopic fields. The

micro-architecture is represented using the concept of a Representative Volume Element (RVE), whose geometry and distribution of constituents must be statistically representative of the micro-scale. In the present case, the micro-scale domain is modelled by a unit cell of lattice structures. The term RVE is avoided here since the unit cell size approaches the limit of the Principle of Scale Separation, required to define an RVE. The applicability of traditional first-order homogenisation is limited by a strong separation of the scales, which may not be verified in architected materials. Second-order homogenisation relaxes the Principle of Scale Separation and introduces an implicit characteristic length (Rodrigues Lopes and Andrade Pires, 2022b), making it better suited for the analysis of materials showing size effects.

Therefore, second-order homogenisation and other multi-scale theories based on generalised continua that include strain gradients have been employed to model architected materials. Nguyen and Noels (2014) investigated the micro-buckling of thin components and macroscopic localisation for cellular materials, where the continuous Galerkin method was employed to solve the strain gradient continuum at the macro-scale. Rahali et al. (2015) and dell'Isola et al. (2019) demonstrated that the homogenised model for pantographic metamaterials requires a second gradient continuum model for accurate predictions. Weeger (2021) obtained the effective constitutive parameters for linear elastic second-gradient models of cubic 3D beam-lattice metamaterials. Yang and Müller (2021) and Yang et al. (2022) explored a computational framework based on a second-order asymptotic homogenisation method to capture both stiffening and softening size effects in mechanical architected metamaterials. Wu et al. (2023b) studied non-linear cellular materials and metamaterials using a secondorder computational homogenisation strategy, employing an equivalent homogenised volume to model strain-gradient effects. Recently, dos Santos et al. (2023, 2024) extended a variationally consistent secondorder homogenisation formulation for the analysis of porous materials, implemented it for FE2 analysis, investigated thin-walled architected structures with coupled deformation modes and size effects.

The abovementioned studies are purely computational and the link between additive manufacturing and advanced multi-scale numerical models accounting for size effects remains underexplored, despite being essential to design and investigate the complex behaviour of architected materials. Yildizdag et al. (2020) manufactured pantographic lattice blocks by selective laser sintering, performed three-point bending tests and showed the accuracy of second gradient models, but size effects have not been addressed. Ciallella et al. (2023) performed a similar analysis, employing Digital Volume Correlation to obtain more detailed comparisons between numerical and experimental results, further emphasising the ability of strain gradient models to capture exotic curvature modes due to the coupling elongation and flexural deformations. For instance, Korshunova et al. (2021) studied the bending behaviour of additively manufactured octet-truss lattice structures - fabricated using SLM technology with stainless steel powder SS 316L-0407 - through experimental validation and numerical modelling via finite element analysis and the Finite Cell Method, incorporating higher-order continuum theories to account for size effects. Aziz et al. (2021) investigated size effects on the mechanical properties of 3D-printed body-centred cubic lattice structures - manufactured using the FFF technique with polymer PLA - coupling mechanical experiments and classical finite element analyses. More recently, Molavitabrizi et al. (2023) employed periodic second-order homogenisation to obtain the properties of an effective strain-gradient continuum representative of a cubic lattice material that was produced using Multi Jet Fusion technology with polyamide PA-12. They explored size effects observed under three-point bending computationally, with DNS and strain-gradient isogeometric simulations, but the experimental results have been obtained for one unit cell size, limiting the numerical validation. Furthermore, as observed in dos Santos et al. (2024), effective properties may vary with the unit cell deformation and that effect can only be captured with finite strain coupled multi-scale simulations. A research question the

still remains is whether the predictions of size effects obtained with different classes of numerical models accurately model the physical behaviour, or not, and what are their limitations.

Therefore, a detailed experimental and numerical study of size effects, combining three-point bending experiments of two lattice structures with advanced modelling strategies, including DNS and secondorder FE² simulations, is presented here. The lattice structures' specimens are manufactured using a more affordable approach that combines FDM 3D printing technique with a commercially available PETG filament, which is a material flexible, strong, simple to print and wellsuited for different applications, such as mechanical parts, printer parts, and protective components (Iftekar et al., 2023). In the authors best knowledge, a direct comparison between experimental and numerical analysis for lattice beams 3D printed with FDM and PETG filament, encompassing different unit cell sizes, has not been performed before. This is fundamental to address the research question. Therefore, specimens have been manufactured and tested while maintaining constant macroscale dimensions and solid volume fraction, but with varying unit cell sizes. Their mechanical response, including reaction curves, strength values and failure mode are analysed in detail. All the experiments are modelled using an in-house finite element code, employing three modelling strategies: (i) DNS finite element models, and (ii) coupled multi-scale strategies based on first-order homogenisation and (iii) also based on second-order computational homogenisation through the recent variational framework developed by dos Santos et al. (2023). In particular, this second-order approach accounting for a scale parameter, in which RVE-based kinematic constraint, including the periodic and minimal models, are systematically derived. It is worth mentioning that three-dimensional FE² multi-scale second-order analyses remain scarcely explored in the computational modelling of the mechanical behaviour of additively manufactured lattice materials with size effects. The impact of macroscopic mesh refinement, of particular importance in the context of second-order analyses, is evaluated in multi-scale simulations. Lattice morphologies with different solid material configurations at the outer boundary of the unit cell were investigated to evaluate the effect of micro-scale boundary conditions applied to the unit cell models in multi-scale analyses. Thus, the comparative analysis of numerical results enables the assessment of accurate models for capturing size effects in additively manufactured architected structures, along with the advantages and limits of applicability of each modelling strategy. Moreover, coupling 3D printing with advanced modelling options represents a powerful approach towards enhancing the design and fabrication of architected structures in order to achieve the desired mechanical properties.

In summary, this paper is organised as follows. Details of the characterisation of the mechanical properties of the printed PETG, along with the main aspects of 3D printing and the experimental and computational methods to perform and simulate three-point bending tests of two different architected structures, are presented in Section 2. The experimental and numerical results, the latter encompassing both DNS and FE² strategies, are presented in Section 3, focusing on the reaction curves, failure mode and size effects. A critical comparison of the numerical results, using the experimental observations for their assessment, is performed in Section 4. presents the results and discussion focusing on size effects on the mechanical behaviour of the studied structures, including a comparison between the experimental and numerical responses. Finally, Section 5 summarises the main conclusions of this experimental and numerical study.

2. Material and methods

2.1. Additive manufacturing of architected structure by FDM

The FDM-based additive manufacturing method was chosen to fabricating the architected structures. This technique enables the creation of complex and customised geometries for polymer-based materials. Since

Table 1Material properties of the commercially available PETG filament (feedstock) provided by the manufacturer (3D Lab, Brazil).

Material properties of the PETG filament	Value	Method
Density	1.27 g/cm ³	ASTM D792
Fusion temperature	240 °C-260 °C	ASTM D3418
Glass transition temperature or Tg	70 °C	ASTM D1525
Modulus of elasticity	2100 MPa	ASTM D790
Tensile stress at yield	50 MPa	ASTM D638
Flexural strength	70 MPa	ASTM D790
IZOD impact strength	101 J/m	ASTM D256

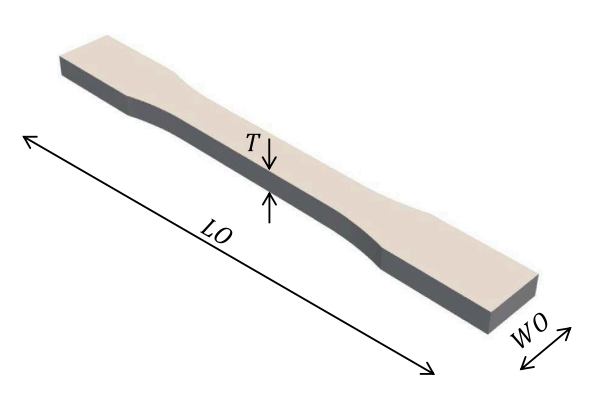
FDM offers flexibility in material selection, it allows for the choice of thermoplastic materials tailored to achieve the mechanical, thermal, and chemical properties required for specific applications of architected structures. Furthermore, FDM is generally more affordable due to lower equipment and material costs when compared to other additive manufacturing techniques. The Sethi3D AiP A3 printer, equipped with a direct drive extruder and a brass nozzle (0.4 mm), was used for all 3D printing of the architected structures and standard test specimens (material characterisation).

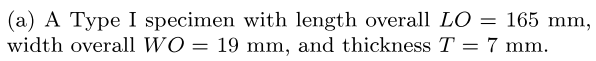
A commercially available PETG filament with uniform opaque colour supplied by the manufacturer 3D Lab (Brazil) was selected as the feedstock for the 3D prints. This amorphous polymer, commonly used in additive manufacturing, also offers other attractive features, such as good printability, cost-performance efficiency, a balanced combination of strength and deformability, and chemical resistance, among others. The typical material properties of the filament provided by the manufacturer are shown in Table 1. Simplify3D software was used to control the printing process by converting 3D CAD models into G-code. After conducting calibration tests, the following printing parameters were defined: (i) heatbed temperature of 75°, (ii) nozzle temperature of 250°, (iii) infill 100% rectilinear 0°/90° (xy plane), (iv) layer height of 0.2 mm, (v) extrusion factor of 0.96, (vi) three perimeters, and (vii) print speed of 50 mm/s.

2.2. Characterisation of the mechanical properties of the printed polymer

Even though the PETG filament's mechanical properties are provided, the mechanical properties of the printed polymer depend on the printing conditions. Therefore, characterisation tests are conducted on standardised specimens, following ASTM D638, produced with the same printing conditions employed to manufacture the lattice structures to obtain realistic properties of the base material that can be used in the numerical models. The uniaxial tensile tests were carried out using five type I specimens with length overall LO = 165 mm, width overall WO = 19 mm, and thickness T = 7 mm (see Fig. 1). The set of tensile tests aimed to determine the modulus of elasticity (*E*), tensile stress at yield (σ_0), tensile strength at failure (σ_b), and elongation at failure (ε_b) . The tests were conducted at a speed of 5 mm/min using an Instron 5969 Dual Column Testing System equipped with a 5 kN load cell. As shown in Fig. 2(a), a mechanical strain gauge was employed to measure the longitudinal deformations. Fig. 2(b) shows the broken test specimens after the uniaxial tensile tests. The results depicting the constitutive behaviour in terms of tensile stress versus tensile strain (σ_t versus ε_t) are presented in Fig. 3. The results of material characterisation of five Type I specimens manufactured with PETG by 3D printing are shown in Table 2.

The average results for each material parameter are presented in Table 3, including the standard deviation (SD) and the coefficient of variation (CV). In particular, the experimental data associated with the Poisson's ratio (ν) were obtained by dos Santos et al. (2025), where an optical extensometer-based method was employed to measure the transverse and longitudinal deformations of Type I test specimens fabricated with PETG from the same manufacturer (3D Lab, Brazil). It is important to note that the elastic parameters E and ν are essential for performing elastic finite element numerical simulations of architected structures manufactured via FDM-based 3D printing.







(b) Five 3D-printed specimens of type I for material characterisation.

Fig. 1. Type I specimens for uniaxial tensile test.



(a) 3D-printed specimen under uniaxial tensile test.



(b) Broken test specimens.

Fig. 2. Uniaxial tensile tests for five Type I specimens.

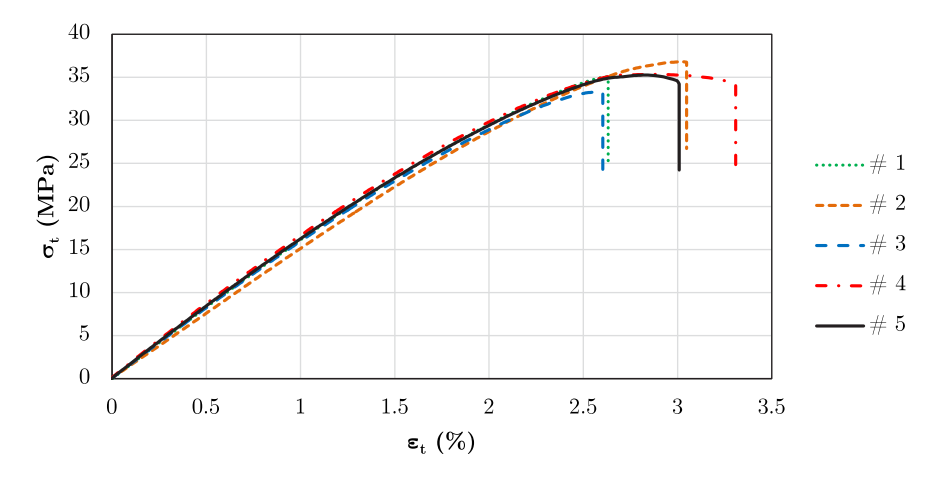


Fig. 3. Tension stress versus tensile strain (σ_i versus ε_i) for uniaxial tensile test considering five test specimens (# 1, # 2, # 3, # 4 and # 5).

Table 2Mechanical properties from tensile tests of five 3D-printed Type I specimens manufactured with PETG.

Specimen	E# (MPa)	$\sigma_{max}^{\#}$ (MPa)	$\sigma_b^{\#}$ (MPa)	$arepsilon_b^{\#}$
# 1	1654	35.07	34.97	2.63%
# 2	1519	36.80	36.74	3.05%
# 3	1652	33.28	33.05	2.60%
# 4	1747	35.33	34.05	3.31%
# 5	1690	35.26	34.22	3.01%

Table 3

Mechanical properties from tensile tests of 3D-printed Type I specimens manufactured with PETG.

Mechanical properties	Value	SD	CV
E	1652 MPa	83.61 MPa	5.06%
$v^{\mathbf{a}}$	0.33	0.08	24.71%
σ_{max}	35.15 MPa	1.25 MPa	3.56%
σ_b	34.61 MPa	1.36 MPa	3.97%
$oldsymbol{arepsilon}_b$	2.92%	0.30%	10.33

^a Value reported by dos Santos et al. (2025).

Table 4 Solid volume (V_{tt}^s) and solid volume fraction (f_{tt}^s) for lattice beams.

Geometry	Beam	V_M^s (mm ³)	f_M^s
	Model 1 (UC Size 1)	61 440	0.64
Triangle-shaped	Model 2 (UC Size 2)	61 440	0.64
	Model 3 (UC Size 3)	61 440	0.64
	Model 1 (UC Size 1)	61 440	0.64
Square-shaped	Model 2 (UC Size 2)	61 440	0.64
	Model 3 (UC Size 3)	61 440	0.64

2.3. Specimens and experimental apparatus for three-point bending tests

Three-point bending experimental mechanical tests were conducted for two sets of architected structures: (i) lattice beams composed of with a triangle-shaped micro-architecture unit cells (triangular lattice, see Fig. 4), and (ii) lattice beams composed of unit cells with a squareshaped micro-architecture (square lattice, see Fig. 5). The beams have equal overall dimensions, with a longitudinal length of $L_x = 240 \text{ mm}$ and a cross-section of $L_v = 20$ mm by $L_z = 20$ mm. Regarding the setup for the three-point bending test, a distance of $L_s = 200$ mm is set between the two supports at the bottom of the lattice beams. To assess the size effect on the architected structures, three specimen configurations were designed for each type of lattice, considering different unit cell (UC) sizes, denoted by l_u . The specimen configurations are characterised by: (I) UC size 1 (l_{μ} = 20.00 mm), composed of 12 unit cells (12 \times 1 \times 1), (II) UC size 2 (l_{μ} = 10.00 mm), composed of 96 unit cells (24 \times 2 \times 2), and (III) UC size 3 ($l_u = 6.67$ mm), composed of 324 unit cells (36 \times 3 \times 3). Cellular beam specimens with more unit cells (i.e., more refined micro-architected arrangements) were discarded due to poor 3D print quality, which highlighted the limitations of the equipment and technique used in the fabrication

It is worth noting that the unit cells and lattice beams have the same total solid volume fraction (i.e., only the unit cell size is modified). Tables 4 and 5 present details of the solid volume and solid volume fraction for lattice beams and unit cells, respectively. Furthermore, the solid outer surface area of the triangular-shaped unit cell (A_{outer}^{Δ}) is 22.73% lower than that of the square-shaped unit cell (A_{outer}^{Δ}) , i.e., $A_{outer}^{\Delta} = 0.7727 A_{outer}^{\Box}$. The compared area values encompass the outer solid surfaces of the unit cells, including the front, back, left, right, top, and bottom faces (see details in Fig. 6 and Table 6).

Figs. 7 and 8 present photos of the 3D-printed architected specimens, illustrating the different configurations manufactured for both triangular and square lattice beams, respectively. Three test specimens

Table 5 Solid volume (V_s^s) and solid volume fraction (f_s^s) for unit cells.

Geometry	UC	V_{μ}^{s} (mm ³)	f^s_μ
	Size 1	5120.00	0.64
Triangle-shaped	Size 2	640.00	0.64
	Size 3	189.63	0.64
	Size 1	5120.00	0.64
Square-shaped	Size 2	640.00	0.64
	Size 3	189.63	0.64

were printed for each beam configuration to assess the representativeness of the mechanical results. Three-point quasi-static bending tests were performed on a universal testing machine (Instron 5969 Dual Column Testing System) at a speed of 2 mm/min, using a 5 kN static load cell. The load cell was positioned in the centre of the lattice beams. The purpose of the experimental tests is to obtain the mechanical behaviour associated with flexural stress versus flexural strain curves ($\sigma_f \cdot \varepsilon_f$). Finally, Figs. 9 and 10 show the lattice beam models positioned for the three-point bending tests.

2.4. Modelling strategies for numerical simulation of the three-point bending test

Computational modelling is carried out through numerical simulations in an in-house FEM code using a computer with an Intel® Xeon® E5-2650 v4 processor, consisting of 24 physical cores (48 virtual cores) and 128 GB of RAM, which was used to conduct the numerical analyses. Initially, conventional simulations were conducted by full-scale DNS models, where the architected structure is represented in detail through an arrangement of unit cells. Afterwards, coupled multi-scale FE² simulations, incorporating first- and second-order computational homogenisation, were performed employing the unit cell concept (UC) to model the underlying architected microstructure. All simulations were conducted under the assumption of finite strains within a geometrically nonlinear setting. The matrix material was modelled using a hyperelastic constitutive law, which establishes a linear relationship between the Kirchhoff stress tensor τ and the logarithmic strain tensor ε , defined via the elastic tensor \mathbf{D}^e :

$$\tau = \mathsf{D}^e \, : \, \varepsilon, \tag{1}$$

$$\varepsilon = \ln\left(FF^{T}\right). \tag{2}$$

Moreover, the first Piola–Kirchhoff stress tensor P, which is used in the homogenisation formulation (see Eq. (4)), can be written as follows:

$$P = \tau F^{-T} = (D^e : \ln(FF^T)) \cdot F^{-T}, \tag{3}$$

with \boldsymbol{F} denoting the deformation gradient. In elastic phenomena are not considered in the simulations.

2.4.1. DNS - Direct numerical simulations

The geometry of the DNS models for the architected structures consists of an arrangement of periodic unit cells. Four different DNS models of lattice beams were used in the three-point bending numerical tests: (I) DNS model with UC size 1, containing 12 unit cells (12 × 1 × 1), (II) DNS model with UC size 2, containing 96 unit cells (24 × 2 × 2), (III) DNS model with UC size 3, containing 324 unit cells (36 × 3 × 3), and (IV) DNS model with UC size 4, containing 768 unit cells (48 × 4 × 4). Therefore, the structures are made of unit cells with different sizes ($l_{\mu}=20$ mm, $l_{\mu}=10$ mm, $l_{\mu}=6.67$ mm and $l_{\mu}=5.00$ mm), following the 3D-printed models (see Figs. 4 and 5) with the addition of a smaller unit cell size. However, memory limitations of the computer used for processing the numerical simulations did not allow the simulation of the full DNS model with UC size 4. Therefore, symmetry conditions on the x–y and y–z planes were imposed on this DNS model to reduce the computational cost, resulting in 192 unit

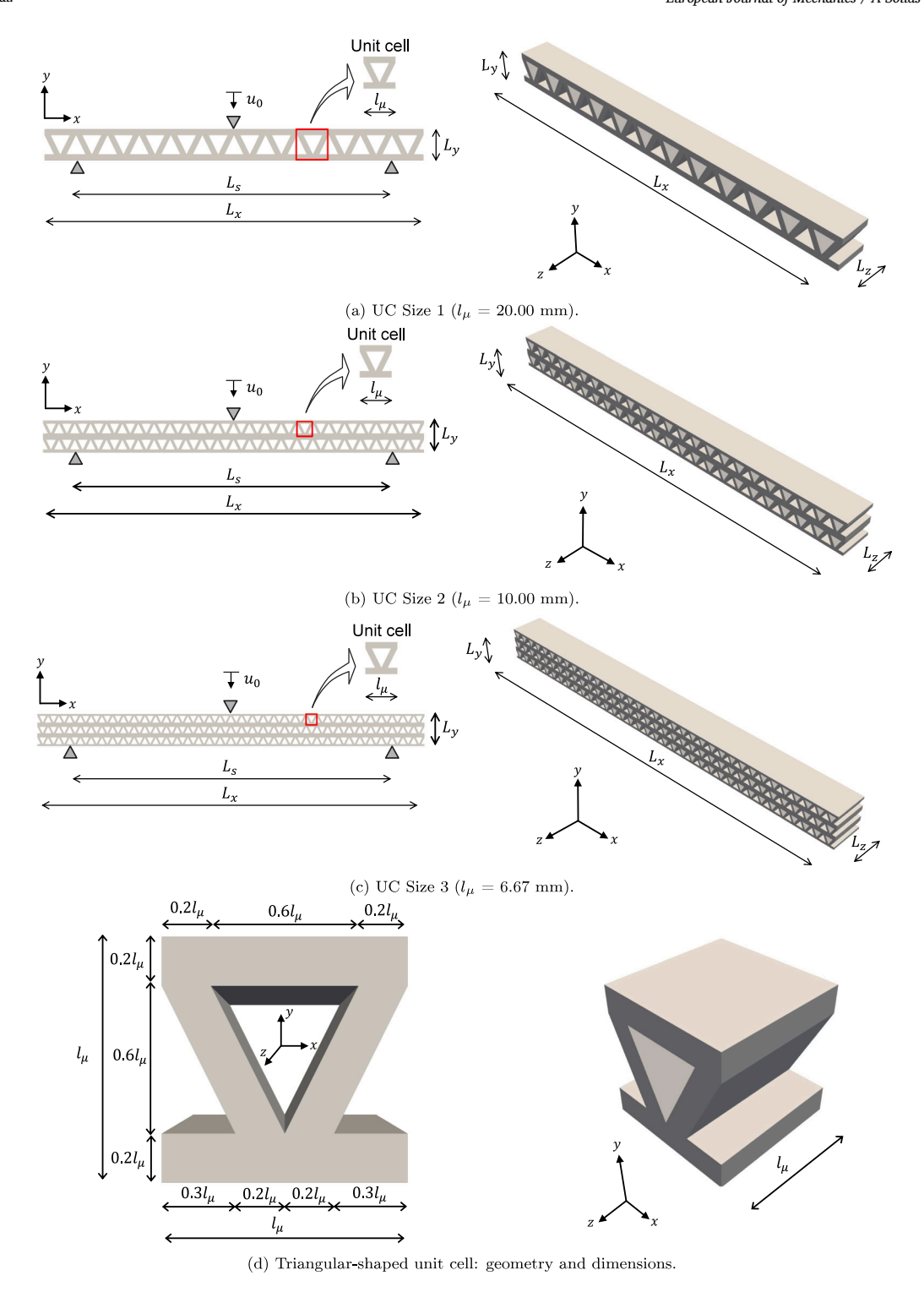
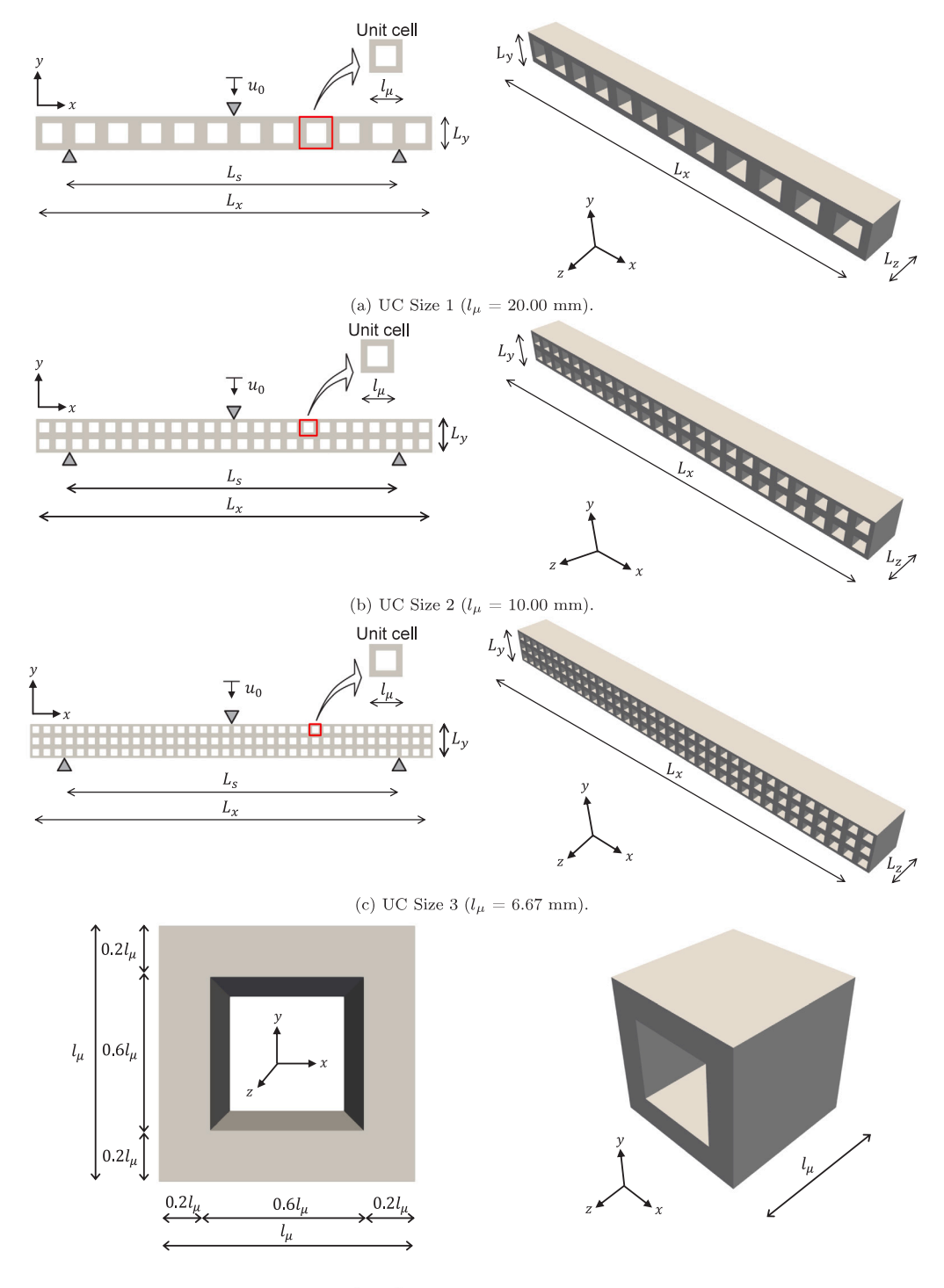


Fig. 4. Dimensions ($L_x = 240$ mm, $L_s = 200$ mm, $L_y = 20$ mm and $L_z = 20$ mm) and boundary conditions for architected structures with triangular-shaped unit cells.

Table 6
Outer surface areas for unit cells.

UC geometry	Case	Outer surfa	Outer surface areas (mm²)					
		Front	Back	Left	Right	Тор	Bottom	Total
	Size 1	256.00	256.00	160.00	160.00	400.00	400.00	1632.00
Triangle-shaped	Size 2	64.00	64.00	40.00	40.00	100.00	100.00	408.00
	Size 3	28.44	28.44	17.78	17.78	44.44	44.44	181.32
	Size 1	256.00	256.00	400.00	400.00	400.00	400.00	2112.00
Square-shaped	Size 2	64.00	64.00	100.00	100.00	100.00	100.00	528.00
-	Size 3	28.44	28.44	44.44	44.44	44.44	44.44	234.64



(d) Square-shaped unit cell: geometry and dimensions.

Fig. 5. Dimensions ($L_x = 240$ mm, $L_y = 200$ mm, $L_y = 20$ mm and $L_z = 20$ mm) and boundary conditions for architected structures with square-shaped unit cells.

cells ($24 \times 4 \times 2$). The difficulty in modelling more refined unit cell arrangements highlights the limitation of DNS models, where a high computational cost, primarily in terms of memory requirements, arises due to the large number of degrees of freedom needed to discretise the lattice structures. Twenty-node hexahedral finite elements (H20) with 8 integration points were used for mesh discretisation of DNS models. Figs. 11 and 12 illustrate the mesh of the DNS models with UC size 1, for the triangular and square lattice beams, respectively. The details of the finite element meshes for all DNS models are provided in Tables 7 and 8. Regarding the loading programme applied to the lattice

beams, a prescribed vertical displacement of $u_0=6.0~\mathrm{mm}$ is imposed in 10 equally-spaced increments, simulating the load cell used in the experimental test.

2.4.2. FE^2 – multi-scale simulations based on first- and second-order homogenisation

Fig. 13 presents an illustrative scheme of multi-scale approaches based on first- and second-order computational homogenisation for a porous solid. In this case, two scales are considered for the multi-scale representation of the non-homogeneous material: (i) the macro-scale or

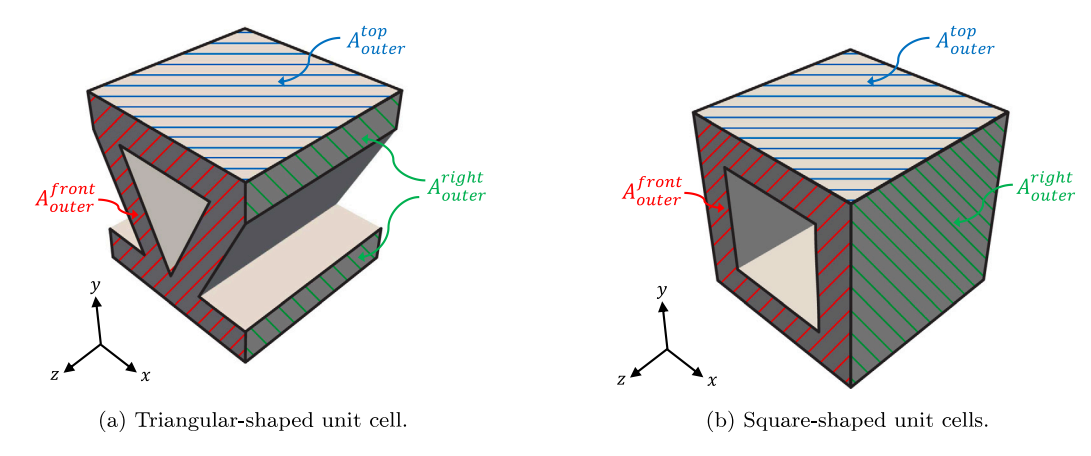


Fig. 6. Representation of outer solid surface areas for unit cells.

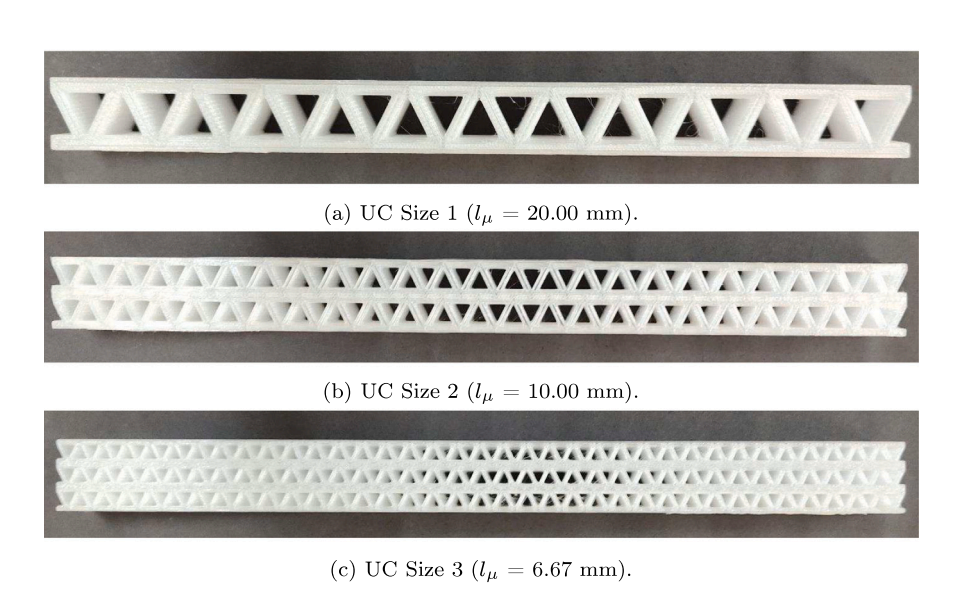


Fig. 7. Configurations of 3D-printed triangular lattice beams produced for three-point bending tests.

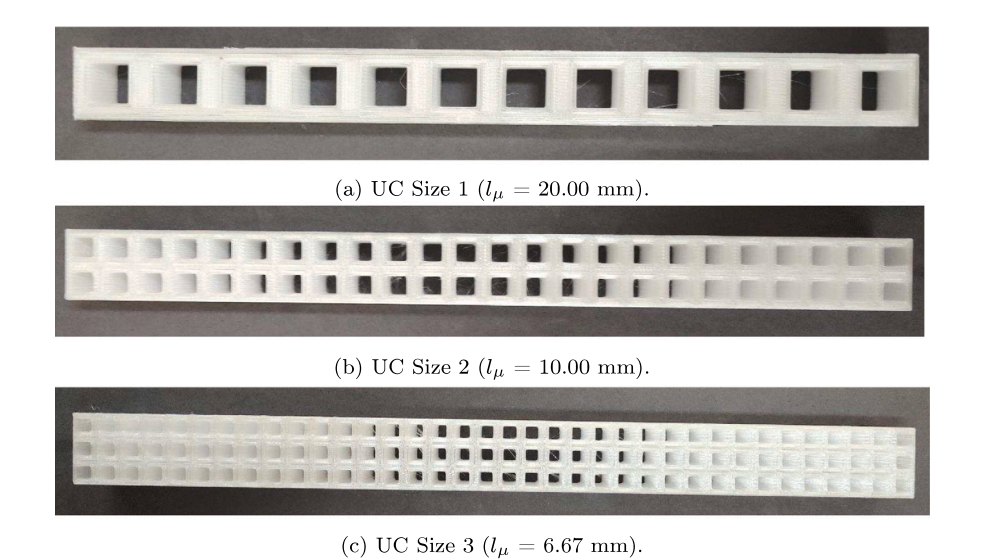


Fig. 8. Configurations of 3D-printed square lattice beams produced for three-point bending tests.

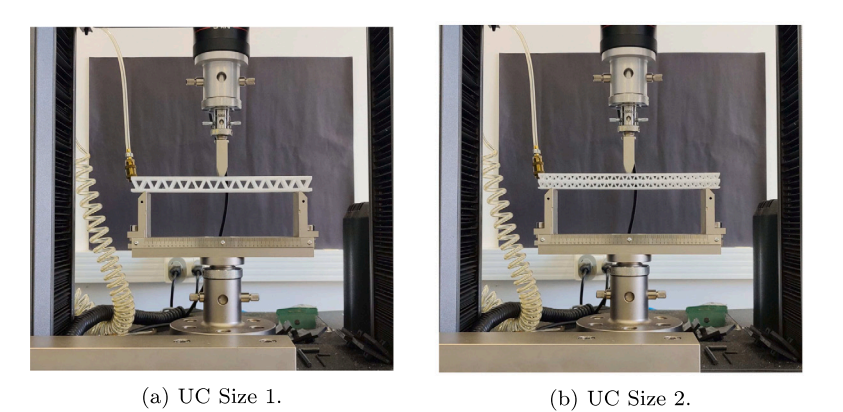




Fig. 9. Experimental apparatus for three-point bending tests on triangular lattice beams.

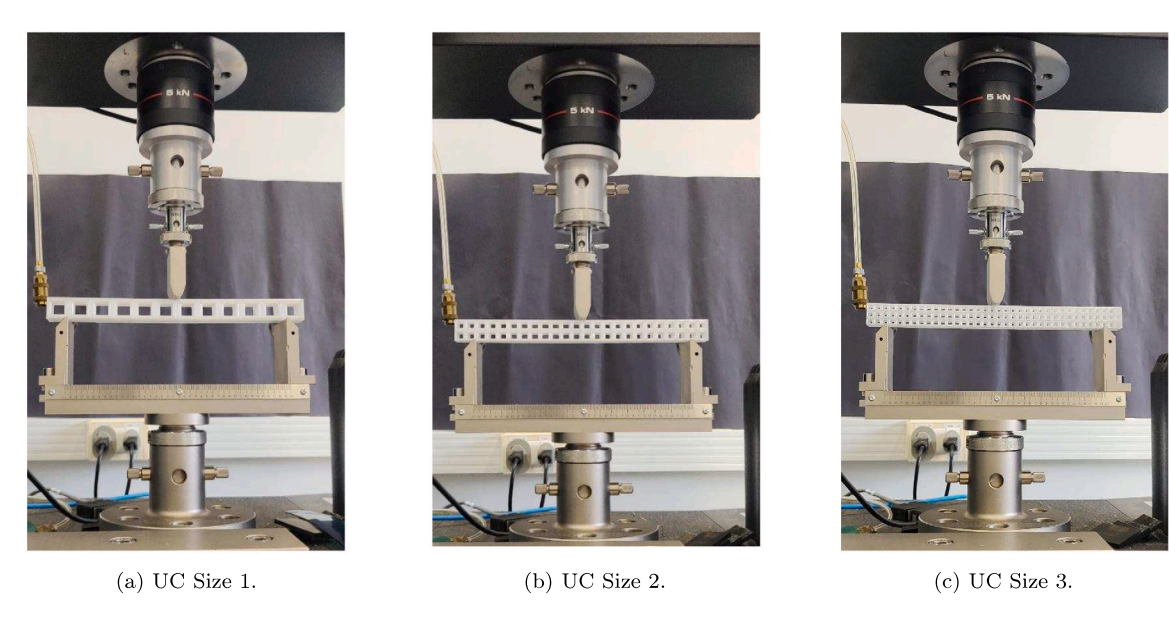


Fig. 10. Experimental apparatus for three-point bending tests on square lattice beams.

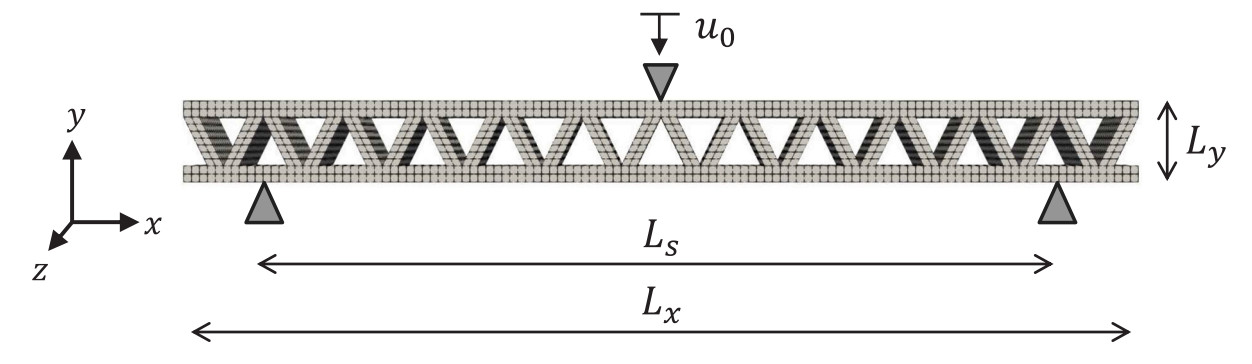


Fig. 11. Finite element mesh of DNS model with UC size 1 (l_{μ} = 20.00 mm), for the triangular lattice beam, with L_x = 240 mm, L_z = 200 mm, L_y = 20 mm and L_z = 20 mm: mesh composed of 8160 elements (H20) and 46274 nodes.

macro-continuum with characteristic length L and domain Ω , and (ii) the micro-scale modelled based on the RVE concept with characteristic length l_{μ} and domain Ω_{μ} , consisting of the solid part Ω^{s}_{μ} and the void part Ω^{v}_{μ} (i.e., $\Omega_{\mu} = \Omega^{s}_{\mu} \cup \Omega^{v}_{\mu}$). Note that each macro-point of the macro-continuum is modelled through an RVE, which incorporates the presence of voids observed at the micro-scale of the non-homogeneous material.

Moreover, u_0 and t_0 indicate the Newman and Dirichlet boundary conditions, respectively, applied at the macro-scale.

In the first-order approach (see Fig. 13(a)), the Cauchy continuum theory (first gradient-based) is assumed for both scales (i.e., macroscale and micro-scale). The macroscopic deformation gradient F is incorporated into the RVE model in the down-scaling process. Then, the RVE equilibrium problem is solved using convenient boundary conditions, which define different multi-scale models. For example, the subsequent multi-scale models can be derived from micro-scale boundary conditions imposed on the RVE (Lopes et al., 2021): (i) uniform traction boundary condition (lower bound); (ii) periodic boundary

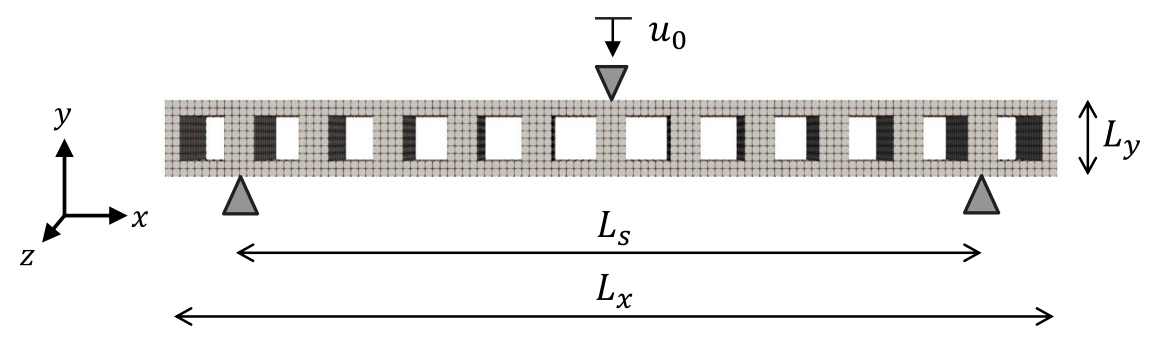


Fig. 12. Finite element mesh of DNS model with UC size 1 ($l_{\mu} = 20.00$ mm), for the square lattice beam, with $L_x = 240$ mm, $L_y = 200$ mm, $L_y = 20$ mm and $L_z = 20$ mm: mesh composed of 7680 elements (H20) and 41561 nodes.

Table 7
Mesh data (H20 element) for DNS models with triangular-shaped unit cells.

DNS	Elements	Nodes
Model 1 - Size 1	8160	46 274
Model 2 - Size 2	65 280	341 995
Model 3 - Size 3	220 320	1 123 324
Model 4 - Size 4 ^a	130 560	669 069

a With symmetry conditions in the x-y and y-z planes.

Table 8
Mesh data for DNS models with square-shaped unit cells.

DNS	Elements (H20)	Nodes
Model 1 - Size 1	7680	41 561
Model 2 - Size 2	61 440	304881
Model 3 - Size 3	207 360	998 761
Model 4 - Size 4 ^a	122880	594841

a With symmetry conditions in the x-y and y-z planes.

displacement fluctuations; (iii) linear boundary displacements (upper bound). Afterwards, the homogenisation process allows obtaining the first Piola–Kirchhoff stress tensor P (the energetic conjugate of F) and the corresponding constitutive consistent tangent A. Since no scale parameter is introduced in this type of approach, the first-order strategy does not capture size effects. It is important to highlight that the Principle of Scale Separation must be satisfied, where the RVE length (micro-scale length, I_{μ}) must be much smaller than the length of the macroscopic structure (i.e., $I_{\mu} \ll L$), so that constant macroscopic deformation gradient can be assumed.

The multi-scale second-order homogenisation is an extension of the first-order homogenisation-based model. In general, the macro-scale is enriched through the consideration of the second-gradient continuum theory (see Fig. 13(b)), while the micro-scale local behaviour is still modelled by the Cauchy continuum theory. In the down-scaling process, the deformation descriptors F and G (second gradient of the displacements) are inserted into the RVE model. An RVE equilibrium problem must also be solved with micro-scale constraints imposed over the RVE, where distinct models can be defined for the multi-scale strategy. For instance, the second-order approach presented by dos Santos et al. (2023) enables the definition of the following multi-scale models from micro-scale constraints imposed on the RVE: (i) minimal constraint (lower bound); (ii) periodic constraint; (iii) direct constraint (upper bound). The homogenisation procedure enables the recovery of the conjugate stresses P and Q (higher-order stress tensor), as well as the respective consistent tangents (A, A_G , H, and H_F). In particular, a characteristic length scale parameter is naturally incorporated in the constitutive relations. As a consequence, the second-order strategy captures size effects, and allows for regularisation of moderate strain localisation (Rodrigues Lopes and Andrade Pires, 2022b). Moreover, the Principle of Scale Separation is relaxed such that the RVE length can

be increased up to a value where a linear evolution of the macroscopic deformation gradient is observed in the RVE.

Further details on first- and second-order multi-scale strategies based on computation homogenisation explored in this work can be found in Lopes et al. (2021) and dos Santos et al. (2023), respectively. In summary, variationally consistent formulations across the scales are derived using the Method of Multi-Scale Virtual Power (Blanco et al., 2016) to define RVE-based multi-scale models. In particular, it is worth mentioning that the first Piola–Kirchhoff stress and the homogenised higher-order stress tensors are obtained through the average-based homogenisation theory, resulting in

$$P = \frac{1}{V_{\mu}} \int_{\Omega_{\alpha}^{s}} P_{\mu} dV, \tag{4}$$

and

$$\mathbf{Q} = \frac{1}{V_{\mu}} \int_{\Omega_{\mu}^{S}} \left(\mathbf{P}_{\mu} \otimes \mathbf{Y} \right)^{S} dV, \tag{5}$$

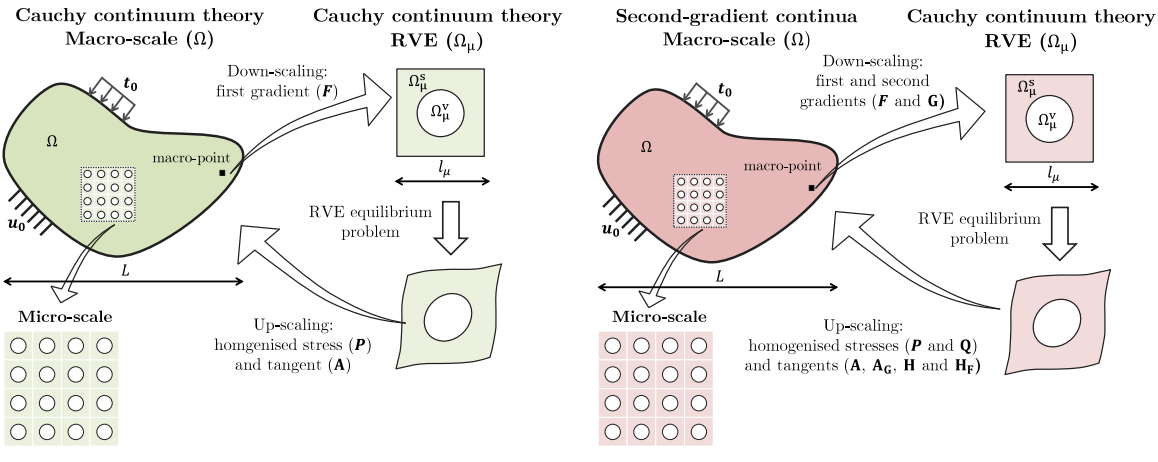
with ${}^{\bullet S}$ denoting the right-hand symmetry operator, Y representing the vector of reference coordinates over the RVE, and V_{μ} indicating the RVE volume.

Furthermore, the homogenised consistent tangents (A, A_G , H, and H_F), which must be defined to solve the non-linear macroscopic equilibrium problem using the Newton–Raphson method, can be derived by

$$A = \frac{\partial P}{\partial F}, \quad A_G = \frac{\partial P}{\partial G}, \quad H = \frac{\partial Q}{\partial G}, \quad H_F = \frac{\partial Q}{\partial F}.$$
 (6)

In this context, coupled multi-scale approaches based on first- and second-order computational homogenisation were also explored for the numerical modelling of the mechanical behaviour of architected structures. Since the lattice structures are composed of arrangements of unit cells, the micro-scale is modelled using the concept of the unit cell (UC) in multi-scale analyses. In the remainder Figs. 14 and 15 present illustrative schemes of multi-scale modelling for three-point bending tests, incorporating geometry, dimensions, and boundary conditions. It is important to note that the UC size has no influence on firstorder multi-scale simulations. On the other hand, a scale parameter is naturally incorporated into the second-order multi-scale formulation presented by dos Santos et al. (2024). To evaluate the influence of the size effect, six different UC sizes (equivalent to the unit cell sizes) were considered at second-order multi-scale simulations: (i) Size 1 (l_{μ} = 20.00 mm), (ii) Size 2 ($l_{\mu} = 10.00$ mm), (iii) Size 3 ($l_{\mu} = 6.67$ mm), (iv) Size 4 (l_{μ} = 5.00 mm), (v) Size 5 (l_{μ} = 3.33 mm), and (vi) Size 6 $(l_{\mu} = 2.50 \text{ mm})$. In this study, the multi-scale simulations enabled the analysis of more UC sizes for lattice beams compared to DNS models that were limited to sizes 1-4 due to computer memory constraints.

FE² multi-scale analyses require finite element simulations at both the macro-scale and micro-scale. First-order coupled multi-scale analyses are conducted using macro- and micro-level meshes composed of H20 elements. On the other hand, second-order coupled multiscale analyses require C¹ continuity to address the second-gradient



- (a) First-order computational homogenisation.
- (b) Second-order computational homogenisation.

Fig. 13. Porous material modelled through multi-scale approaches.

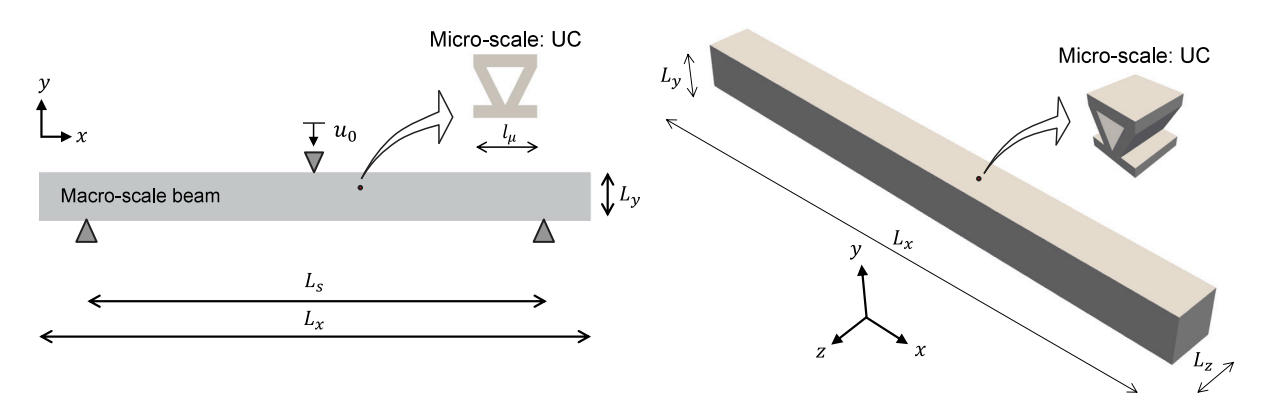


Fig. 14. Multi-scale scheme for determining the homogenised macroscopic behaviour of lattice beams ($L_x = 240$ mm, $L_y = 20$ mm, and $L_z = 20$ mm) with a triangular-shaped UC.

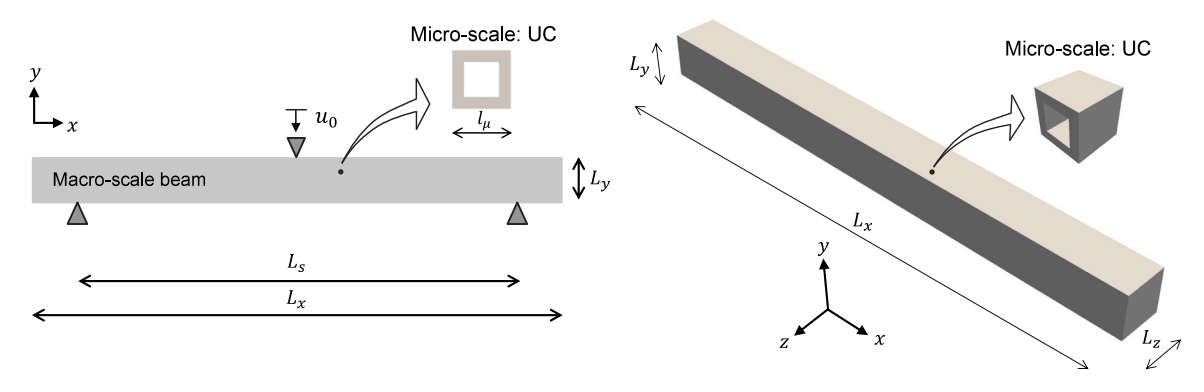
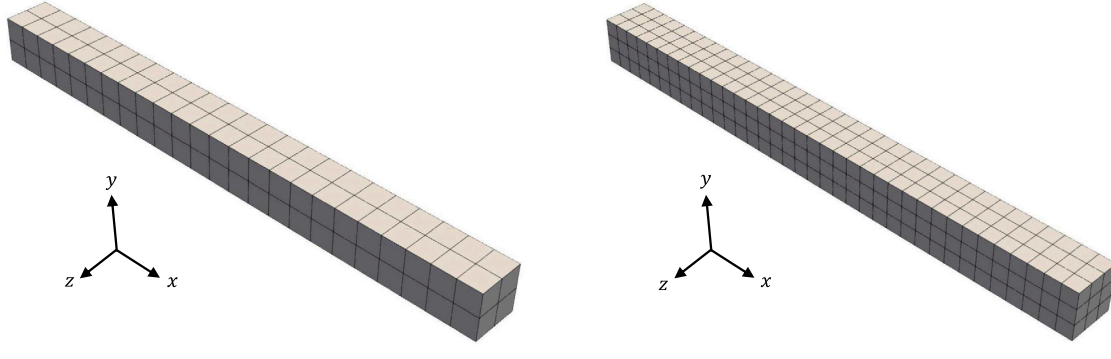


Fig. 15. Multi-scale scheme for determining the homogenised macroscopic behaviour of lattice beams ($L_x = 240$ mm, $L_y = 20$ mm, and $L_z = 20$ mm) with a square-shaped UC.

equilibrium problem. Thus, a mixed finite element named H20F8L1 (hexahedron twenty node-based shape functions, eight linear interpolation functions for the relaxed deformation gradient and constant Lagrange multipliers) was defined for numerical simulations at the macro-scale (see more details in Rodrigues Lopes and Andrade Pires (2022a)). Furthermore, the micro-scale is still adopted as a classical continuum, allowing to use H20 elements for UCs in second-order multi-scale analyses. Details of the macroscopic meshes are shown in

Fig. 16, while the UC mesh data are presented in Figs. 17 and 18. In particular, two meshes are defined at the macro-scale to assess the convergence of the numerical results. The micro-scale meshes have characteristics similar to those defined for the unit cells in the DNS models. A preliminary study using more refined micro-scale meshes revealed minimal impact on the numerical results. In the numerical simulation, the loading program was defined by applying a total prescribed displacement of $u_0=6.0~\mathrm{mm}$ divided into 10 increments. The



(a) Macro mesh composed of 96 elements (H20 or H20F8L1) (b) Macro mesh composed of 324 elements (H20 or and 741 nodes. H20F8L1) and 2056 nodes.

Fig. 16. Meshes studied at the macro-scale for multi-scale simulations.

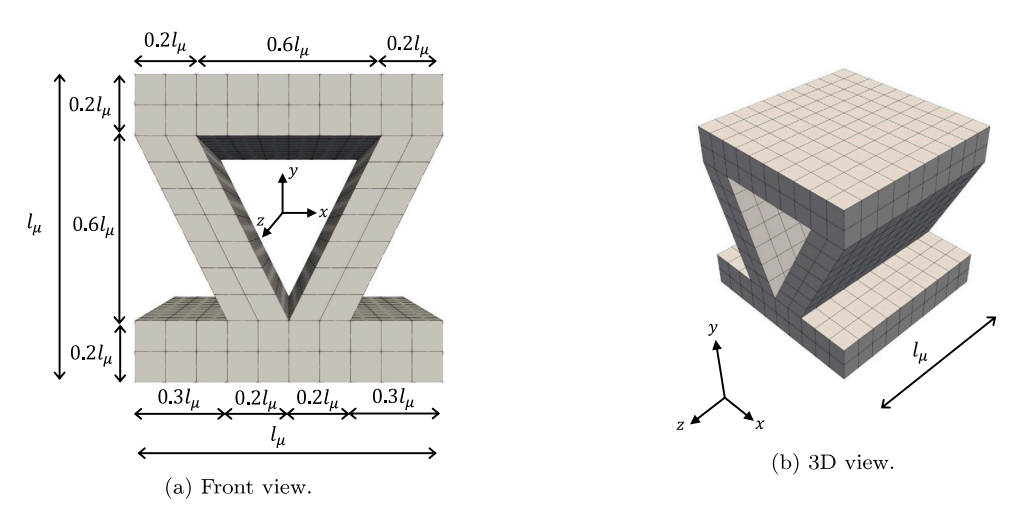


Fig. 17. Triangular-shaped UC: geometry and mesh composed of 680 elements (H20) and 4012 nodes.

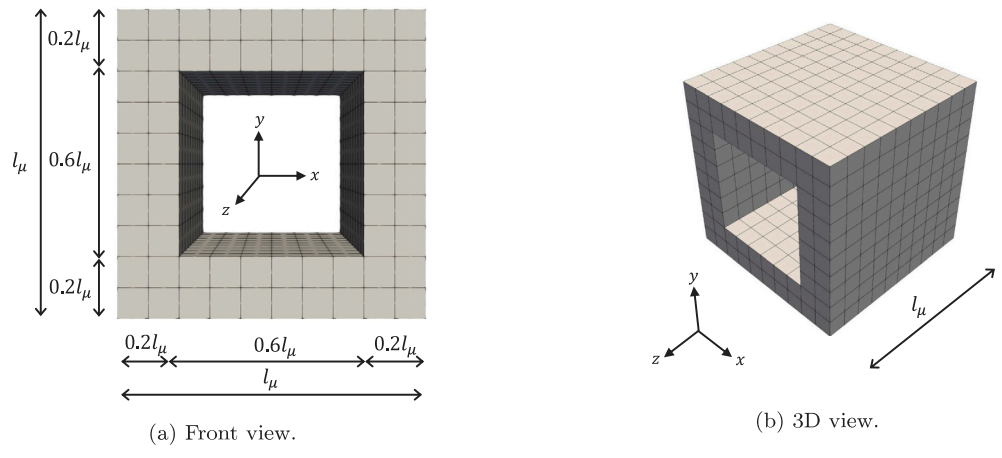


Fig. 18. Square-shaped UC: geometry and mesh composed of 640 elements (H20) and 3776 nodes.

following multi-scale models were employed in the simulations: (i) first-order approach: uniform traction boundary condition and periodic boundary displacement fluctuations; (ii) second-order approach: minimal constraint and periodic constraint. Since upper bound models are too restrictive, the multi-scale models of linear boundary displacement (first-order theory) and direct constraint (second-order theory)

were not explored in this work, contributing to reduce the amount of three-dimensional multi-scale simulations.

3. Results

This section presents the experimental and numerical results obtained for three-point bending of lattice beams, with particular focus

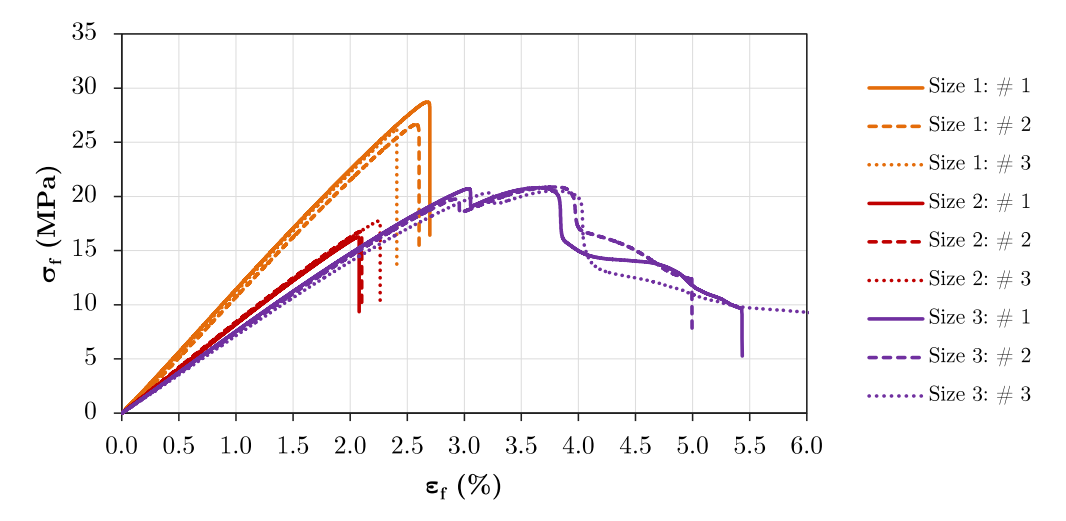


Fig. 19. Experimental results of the mechanical behaviour, considering the flexural stress and the flexural strain $(\sigma_f - \epsilon_f)$ for triangular-shaped structures of size 1, size 2, and size 3 (with # indicating the specimen for each structure).

on size effects. The flexural stress (σ_f) and the flexural strain (ε_f) are calculated as follows:

$$\sigma_{\rm f} = \frac{3RL}{2bd^2},\tag{7}$$

and

$$\varepsilon_{\rm f} = \frac{6Dd}{L^2},\tag{8}$$

where, R and D represent, respectively, the reaction force and the maximum deflection at the centre of the beam, L is the distance between the two outer supports span at the bottom of the beam ($L_s = 200 \text{ mm}$), b is the width of test beam ($L_z = 20 \text{ mm}$), and d is the thickness of tested beam ($L_v = 20 \text{ mm}$).

For the experimental results, in addition to the flexural stress and strain curves, the failure mode is also analysed. The numerical predictions obtained with DNS are briefly compared with the experimental data before failure. Finally, the ${\rm FE}^2$ results are reported for different macroscopic finite element meshes, different formulations (first and second-order homogenisation), and for different micro-scale boundary conditions.

3.1. Experimental results

3.1.1. Triangular lattice

Fig. 19 depicts the experimental curves of flexural stress versus flexural strain $(\sigma_f-\varepsilon_f)$ for 3D-printed lattice beams with a triangular-shaped geometry. This experimental mechanical behaviour is presented for all the manufactured specimen configurations, with UC sizes 1, 2, and 3. In particular, an approximately linear $\sigma_f-\varepsilon_f$ relationship is observed in the experimental results up to $\varepsilon_f=1.8\%$, which justifies the elastic behaviour assumption taken in the numerical models. Moreover, different values of flexural stress are observed at the same level of flexural strain for each case size. At $\varepsilon_f=1.8\%$, the lattice beam with size 1 has superior stiffness, the structure with size 3 is more flexible. Therefore, the experimental investigation indicates that this type of architected structure exhibits the so-called size effect.

On the other hand, the experimental results up to rupture highlight the complexity of the mechanical behaviour of the triangular-shaped lattice beams, manufactured by 3D printing using the FDM technique. In the context of failure analysis, the architected structures of size 1 exhibit superior stiffness and strength, although they show lower ductility. The lattice beams of size 2 display intermediate stiffness, along with lower strength and ductility. Finally, the structures of size 3 exhibit lower stiffness, intermediate strength, and enhanced ductility. Fig. 20 shows the lattice beams with triangular-shaped unit cells near rupture

in the three-point bending experimental tests, where the curvature associated with the bending is visible. Furthermore, Fig. 21 presents the beams after rupture in the experimental tests. The failure occurs near the centre of the architected structure, where the load cell was positioned to apply the prescribed displacement. At around $\varepsilon_{\rm f}=3.0\%$, the lattice beam of size 3 exhibited local buckling in the region of the load cell, which led to localised deformations and contributed to a more ductile rupture compared to sizes 1 and 2. It is worth mentioning that instabilities are commonly observed in architected structures composed of thin-walled elements. However, the modelling of such effects is not addressed in the present work. Further details on addressing local instabilities in three-point bending tests can be found in Yildizdag et al. (2020), for instance. It is worth noting that no strain localisation was observed in the regions near the lower supports.

The local buckling observed for unit cell size 3 shows that Digital Image Correlation (DIC) (Popł awski et al., 2025) and Digital Volume Correlation (DVC) (Ciallella et al., 2023) could be valuable for investigating complex 3D-printed lattice morphologies. For instance, DIC and DVC could provide a more detailed understanding of local micro-deformation fields and the initiation of damage. Thus, these techniques are valuable for enhancing the mechanical characterisation of such artificial structures. In the present study, the lattice structures are designed with unit cell lengths ranging from 20.00 mm to 6.66 mm, which are relatively large when compared to typical microarchitectures. However, future studies will explore structures with more complex morphologies and smaller unit cell lengths, further justifying the incorporation of image-based approaches. Regarding potential limitations, the optical access and resolution required for the successful application of DIC or DVC can still provide experimental challenges, primarily due to the internal geometry and out-of-plane strains in 3D-printed lattice materials.

Table 9 shows the average flexural stress results at a flexural strain of 1.8% (prescribed displacement of 6.0 mm). Although only three specimens of each case size were tested in the laboratory, the low standard deviation and coefficient of variation values indicate good representativeness of the results. Therefore, the 3D printing process using the FDM technique provided good reproducibility of the architected structures in terms of mechanical behaviour.

3.1.2. Square lattice

Fig. 22 presents the experimental mechanical behaviour ($\sigma_{\rm f}$ versus $\varepsilon_{\rm f}$) of 3D-printed square lattice beams with UC sizes 1, 2, and 3. The size effect is also evident in the lattice beams, as different flexural stress values are observed for the same level of prescribed displacement (e.g., see results up to $\varepsilon_{\rm f}=1.8\%$ associated with $u_0=6.0$ mm). In







(a) Beam with size 1.

(b) Beam with size 2.

(c) Beam with size 3.

Fig. 20. Architected structures with triangular-shaped close to rupture in the three-point bending experimental tests.





(a) Beams with size 1 broken.

(b) Beams with size 2 broken.



(c) Beams with size 3 broken.

Fig. 21. Triangular-shaped beams after failure in the three-point bending experimental tests.

Table 9 Averaged experimental flexural stress (σ_f), including SD and CV, for triangular-shaped lattice beams considering $\varepsilon_f = 1.8\%$ ($u_0 = 6.0$ mm).

Configuration	Specimen ID Δ	$\sigma_{\mathrm{f}}^{\scriptscriptstyle\#}$ (MPa)	σ_{f} (MPa)	SD (MPa)	CV
	# 1	20.338			
Size 1	# 2	19.436	19.95	0.466	2.335%
	# 3	20.089			
	# 1	14.478			
Size 2	# 2	14.780	14.65	0.156	1.062%
	# 3	14.694			
	# 1	13.348			
Size 3	# 2	13.129	13.05	0.344	2.633%
	# 3	12.675			

summary, decreasing the unit cell size results in architected structures with reduced stiffness, strength, and ductility. The experimental data indicate curves with an approximately linear behaviour between $\sigma_{\rm f}$ and $\varepsilon_{\rm f}.$ The curvature associated with bending can be observed in Fig. 23, which shows the lattice beams nearing rupture during the experimental tests. As shown in Fig. 24, the failure occurs near the middle of the architected structures. In this case, no strain localisation was observed in the lower regions of the supports or in the upper region corresponding to the position of the load cell.

The average flexural stress value at a flexural strain of 1.8% (prescribed displacement of 6.0 mm) is presented in Table 10. Similar to the triangular lattice beam, only three specimens have been tested for each size but low scatter is obtained in the results. Hence, good reproducibility of the results is also verified in this case.

3.2. DNS results

The mechanical behaviour of the DNS models composed of triangular- and square-shaped unit cells is shown in Figs. 25 and 26, respectively. Note that different unit cell sizes result in distinct flexural stress values, where the reduction in unit cell size leads to lower flexural stress values. Therefore, the size effect is captured through numerical simulations of lattice beams using DNS models. Moreover, the mechanical behaviour demonstrates a linear relationship between the flexural stress and the flexural strain for all cases, revealing that nonlinear geometric effects are not significant for lattice beams under bending. Finally, it is worth mentioning the high computational cost as a disadvantage of DNS models, particularly associated with memory demand, which made simulations of lattice beams with smaller unit cell lengths unfeasible due to the limitation of the processing computer.

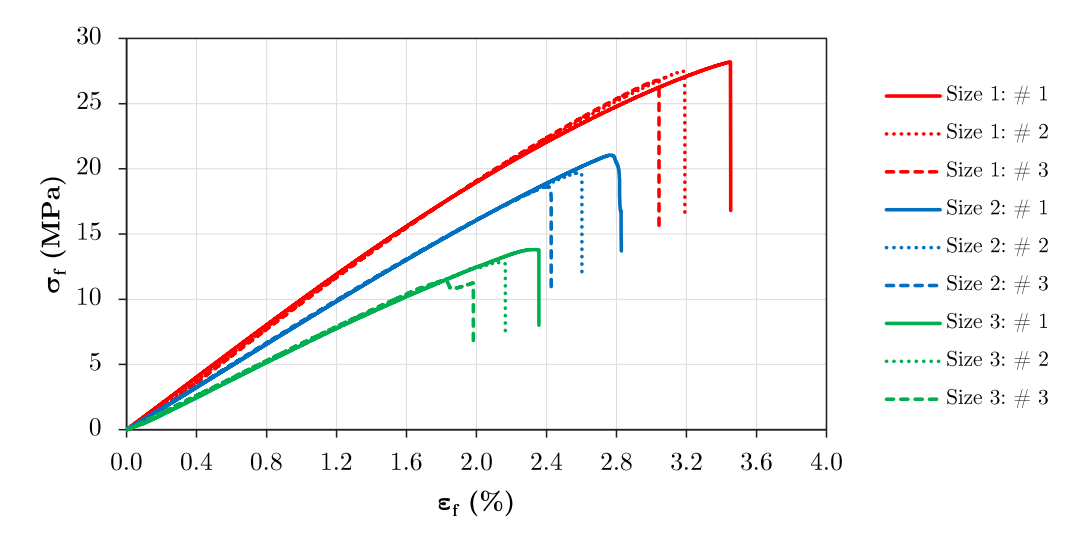


Fig. 22. Experimental results of the mechanical behaviour, considering the flexural stress and the flexural strain $(\sigma_f - \varepsilon_f)$ for square-shaped structures with size 1, size 2 and size 3 (with # denoting the specimen for each structure).

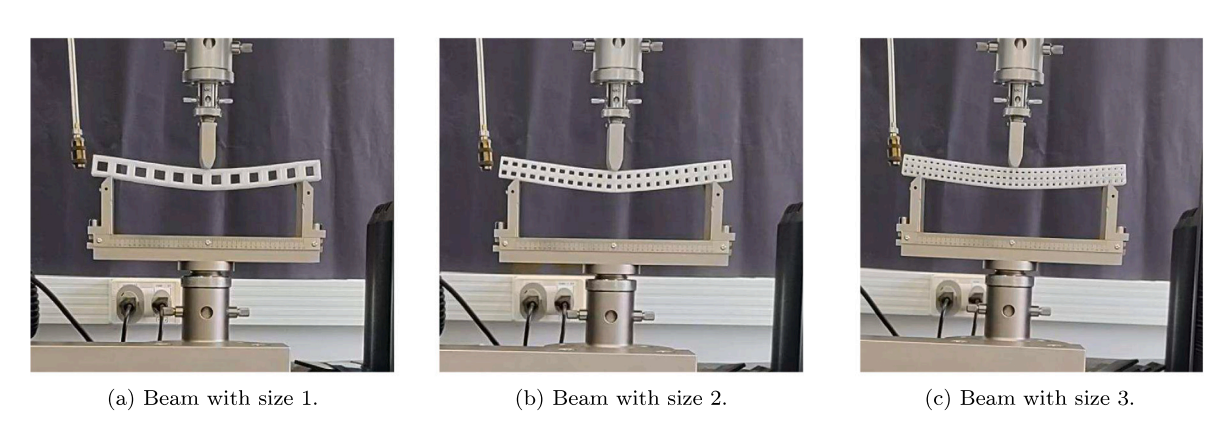
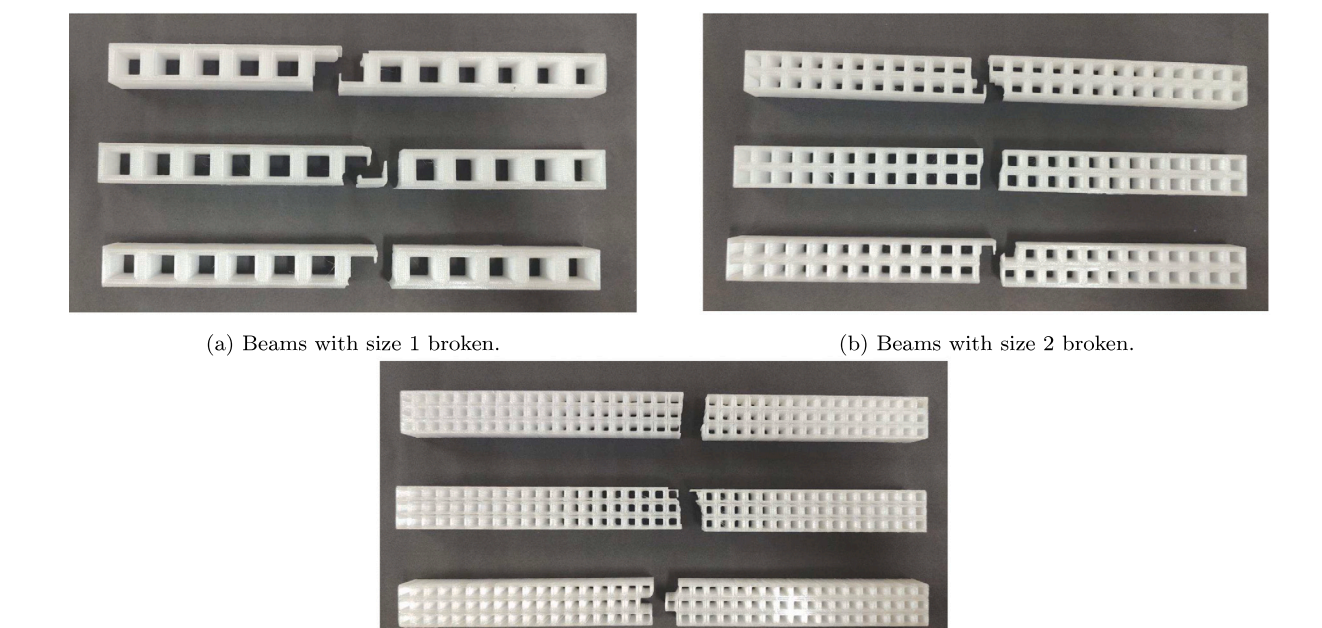


Fig. 23. Architected structures with square-shaped close to rupture in the three-point bending experimental tests.



(c) Beams with size 3 broken.

 $\textbf{Fig. 24.} \ \ \textbf{Square-shaped beams after failure in the three-point bending experimental tests.}$

Table 10 Averaged experimental flexural stress (σ_f), encompassing SD and CV, for square-shaped lattice beams considering $\varepsilon_f = 1.8\%$ ($u_0 = 6.0$ mm).

Configuration	Specimen ID □	$\sigma_{\mathrm{f}}^{\#}$ (MPa)	σ_{f} (MPa)	SD (MPa)	CV
	# 1	17.324			
Size 1	# 2	17.308	17.315	0.008	0.048%
	# 3	17.313			
	# 1	14.571			
Size 2	# 2	14.578	14.586	0.021	0.144%
	# 3	14.610			
	# 1	11.353			
Size 3	# 2	11.417	11.394	0.035	0.309%
	# 3	11.412			

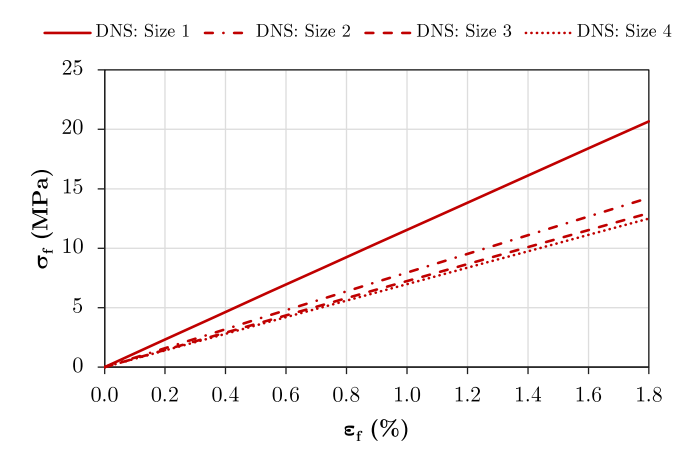


Fig. 25. Mechanical behaviour $(\sigma_f - \varepsilon_f)$ for DNS models composed of triangular-shaped unit cells with sizes 1, 2, 3 and 4.

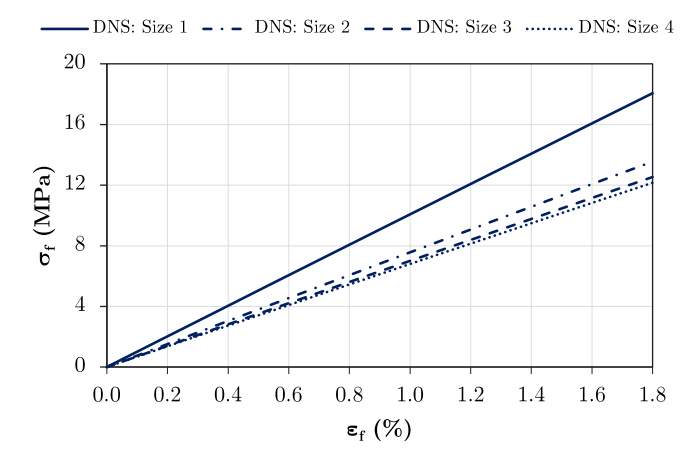


Fig. 26. Mechanical behaviour (σ_f - ϵ_f) for DNS models composed of square-shaped unit cells with sizes 1, 2, 3 and 4.

3.3. Multi-scale results

3.3.1. Macro-scale mesh convergence

Initially, it is important to assess the convergence of numerical responses in FE^2 multi-scale simulations with respect to the finite element mesh. Tables 11 and 12 present a comparison of the flexural stress results for the two investigated macro-scale meshes. In the context of second-order multi-scale simulations, a mesh refinement study was conducted for UC size 3. Since first-order multi-scale analyses are independent of the UC length, the mesh refinement investigation of such models is applicable to all UC sizes. Overall, meshes 1 and 2 yield flexural stresses that are in close agreement, as demonstrated by the small relative differences observed between the meshes. Therefore, to reduce the computational cost of the multi-scale analyses, mesh 1 was

Table 11 Mesh refinement study assessing $\sigma_{\rm f}$ for beams ($\epsilon_{\rm f} = 1.8\%$ associated with $u_0 = 6.0$ mm) composed of triangular-shaped UCs.

Multi-scale model	σ_{f} (MPa)		Differences
	Mesh 1	Mesh 2	
Second-order: Periodic - Size 3	14.49	14.27	1.50%
Second-order: Minimal - Size 3	13.90	13.67	1.65%
First-order: Periodic - All sizes	12.06	12.02	0.28%
First-order: Uniform traction - All sizes	10.11	10.00	1.03%

Table 12 Mesh refinement study assessing $\sigma_{\rm f}$ for beams ($\epsilon_{\rm f}=1.8\%$ associated with $u_0=6.0$ mm) featuring square-shaped UCs.

Multi-scale model	σ_{f} (MPa)		Differences
	Mesh 1	Mesh 2	
Second-order: Periodic - Size 3	14.18	14.05	0.88%
Second-order: Minimal - Size 3	7.01	6.85	2.29%
First-order: Periodic - All sizes	11.79	11.75	0.30%
First-order: Uniform traction - All sizes	4.59	4.58	0.23%

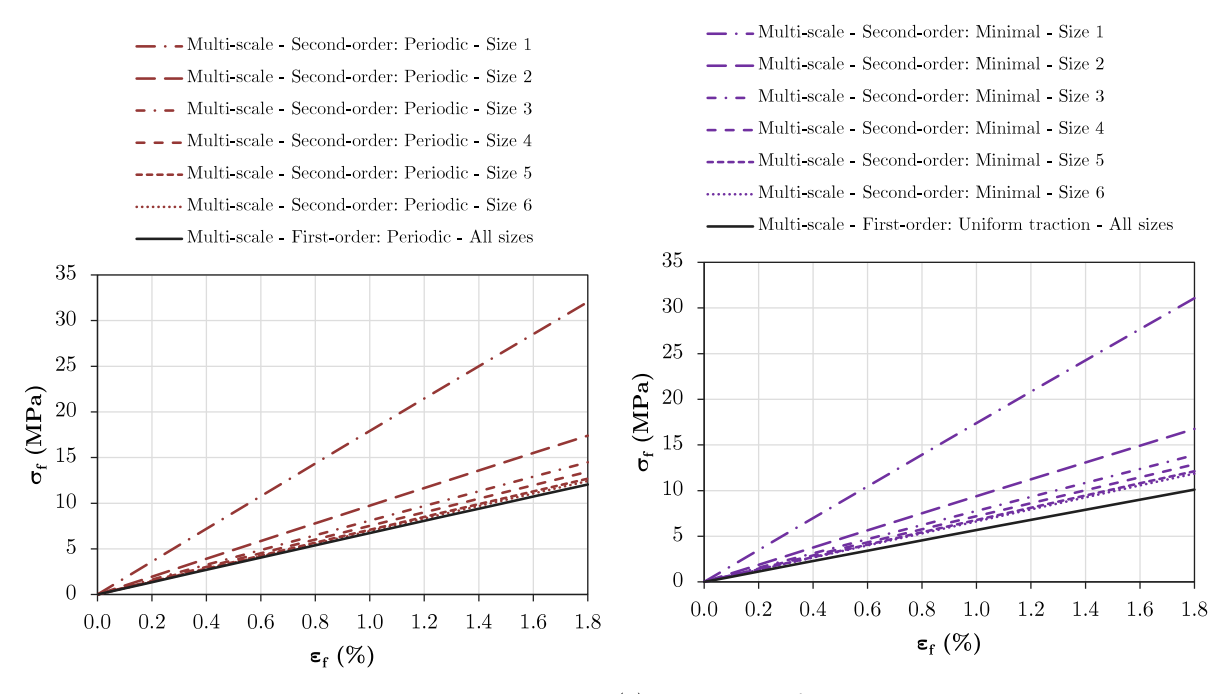
selected for obtaining the remaining numerical results of the lattice beams under bending.

3.3.2. Size effect, multi-scale formulation and type of micro-scale constraint Figs. 27 and 28 show the mechanical behaviour $(\sigma_f - \varepsilon_f)$ of the architected structures from multi-scale simulations, obtained with both first and second-order homogenisation, encompassing different UC sizes and underlying type of micro-scale constraint. Since the numerical results reveal a linear relationship between σ_f and ε_f , geometric nonlinear effects appear to be negligible for the lattice beams under bending. As expected, due to the scale parameter introduced in the formulation, the second-order multi-scale models exhibit mechanical behaviour with a size effect. In summary, increasing the UC size leads to higher flexural stresses for a given level of flexural strain. For smaller UC sizes, the numerical results indicate a convergence of the second-order multiscale models towards the first-order multi-scale models. The type of microscopic constraint also plays a role, with the uniform traction and minimal constraints providing responses that are more compliant, compared to the periodic conditions. A more detailed analysis is provided in Section 4.

4. Discussion of the results

4.1. Influence of unit cell on the experimentally observed size effects

In this section, the size effects observed in the experimental results are discussed, considering the influence of the lattice structure morphology. To that end, the experimental flexural stress obtained at a flexural strain of 1.8% (associated with the enforced displacement of 6 mm), in the three-point bending tests, is analysed with respect to unit cell size ($\sigma_{\rm f}$ versus unit cell length) and architecture of the lattice structure in Fig. 29. It is observed that the triangular lattice beam exhibits a linear relationship between $\sigma_{\rm f}$ and the unit cell size, whereas



- (a) First- and second-order periodic models.
- (b) First-order uniform traction model and second-order minimal model.

Fig. 27. Multi-scale predictions of the mechanical behaviour $(\sigma_{\rm f} - \varepsilon_{\rm f})$ of triangular lattice beams with UC sizes 1 to 6.

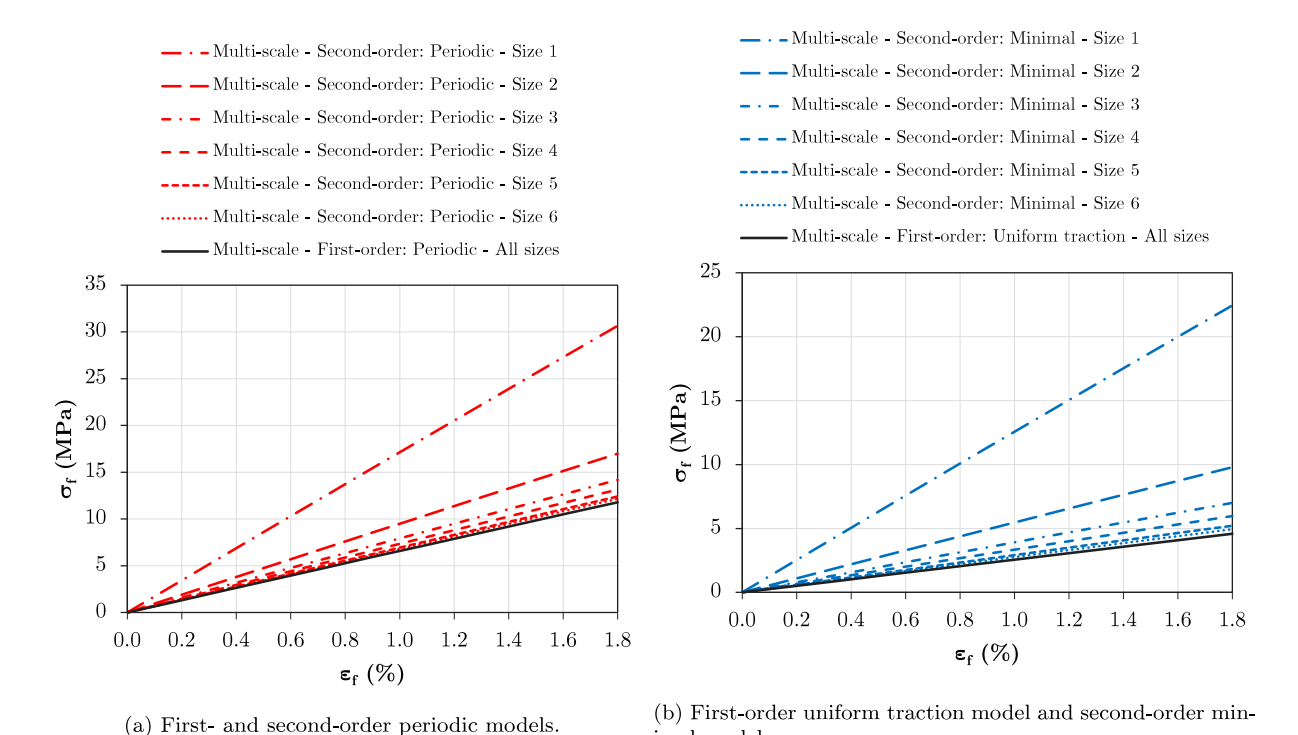


Fig. 28. Multi-scale predictions of the mechanical behaviour $(\sigma_f - \epsilon_f)$ of square lattice beams with UC sizes 1 to 6.

imal model.

this relationship is non-linear for the square lattice beam. Two possible reasons are hypothesised for this difference: (i) the non-linearity is introduced by the geometry of the unit cell or (ii) it is due to the effects of the manufacturing process, such as some anisotropy caused by the printing directions. The analysis of the numerical results will shed some light on this topic.

4.2. Comparison of DNS predictions with experimental results

DNS results and experimental data for lattice beams composed of triangular-shaped unit cells are compared in Fig. 30, with the flexural stress obtained at a flexural strain of 1.8% (prescribed displacement of 6 mm) for different unit cell sizes. Table 13 shows a comparison in more

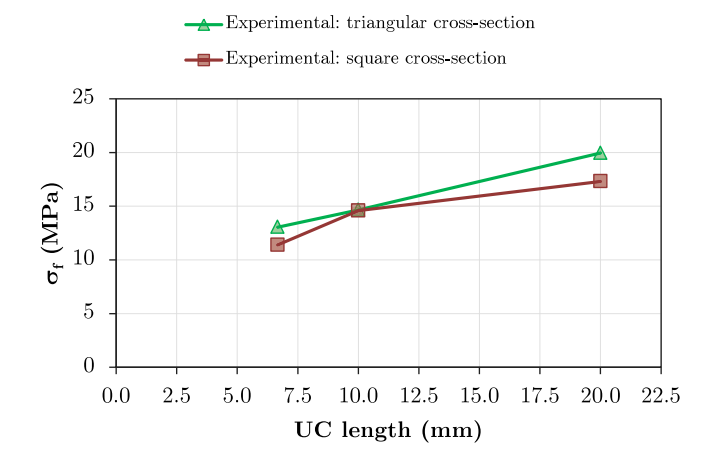


Fig. 29. Size effect experimental study ($\sigma_{\rm f}$ versus UC length) considering $\epsilon_{\rm f}=1.8\%$ ($u_0=6.0$ mm): triangular and square-shaped lattice beams.

Table 13 Comparison of flexural stress for triangular-shaped lattice structures considering $\varepsilon_{\rm f} = 1.8\%$ ($u_0 = 6.0$ mm).

Unit cell	$\sigma_{\rm f}$ (MPa)	Differences		
	Experimental (1)	DNS model (2)	(2) to (1)	
Size 1	19.95	20.66	3.55%	
Size 2	14.65	14.23	2.84%	
Size 3	13.05	12.95	0.75%	
Size 4	_	12.49	_	

detail, including relative differences in modulus (Differences). The comparative study reveals that the DNS predictions are in close agreement with the experimental data, with relative differences lower than 3.5%, demonstrating the robust predictive capability of the full-scale models to capture the size effect in lattice structures. The relationship between flexural stress and unit cell size predicted with DNS is approximately linear, as observed in the experiments. Even though for the lowest unit cell size there is no experimental data, the predicted response follows the trend.

Regarding the square lattice beams, DNS results are compared with experimental data in Fig. 31 and Table 14. Overall, the numerical results of the DNS models are close to the experimental data, although some differences in responses are observed, with larger relative errors, compared to the triangular lattice. DNS predicts an approximately linear relationship for the size effect, which differs from the experimental results. Therefore, considering the hypotheses introduced in Section 4.1, it may be concluded that the non-linear relationship observed in the experiments is not due to the geometrical effects, otherwise these would be captured by the simulation. This may indicate that the manufacturing process significantly influences the experimental investigation of architected structures with different unit cell sizes. In particular, it is noteworthy that some voids were observed in the square-shaped lattice beams composed of unit cells of size 3 (l_u = 6.67 mm), which may have contributed to a reduction in the experimental stiffness of this structure. Thus, differences in results can be attributed to manufacturing defects and the anisotropy induced by the 3D printing process, as well as uncertainties arising from material characterisation.

4.3. Multi-scale results: a comparison with experimental data and DNS predictions

Fig. 32 and Table 15 show the multi-scale simulation results compared to experimental data and DNS predictions for triangular-shaped lattice beams. Furthermore, Table 16 presents a more detailed comparative analysis, including the relative differences (in modulus), between

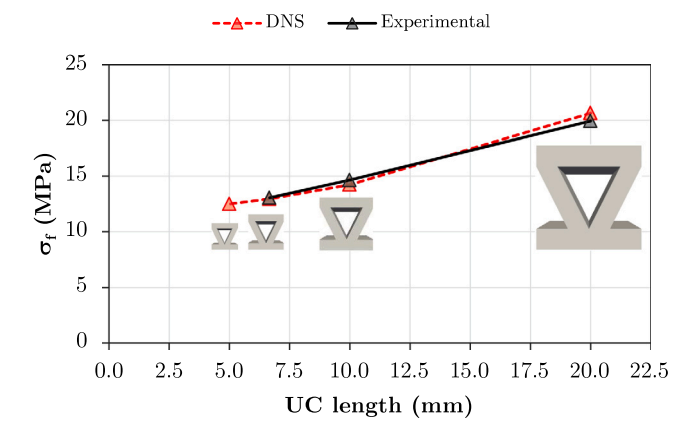


Fig. 30. Size effect study ($\sigma_{\rm f}$ versus UC length) for triangle-shaped structures considering $\varepsilon_{\rm f}=1.8\%$ ($u_0=6.0$ mm): experimental results versus DNS predictions.

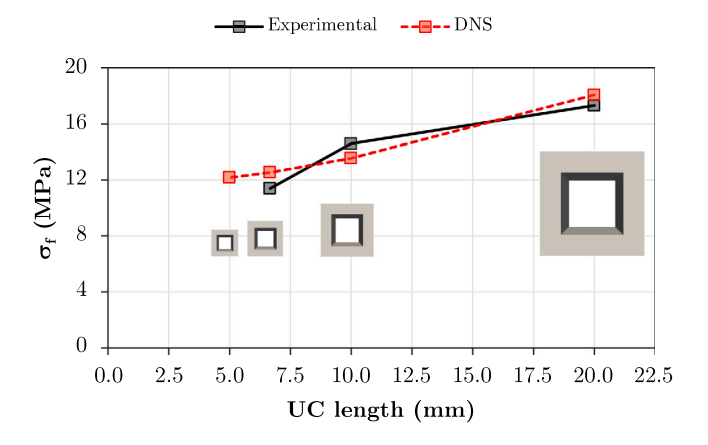


Fig. 31. Size effect study ($\sigma_{\rm f}$ versus UC length) for square-shaped lattice beams considering $\varepsilon_{\rm f}=1.8\%$ ($u_0=6.0$ mm): experimental results versus DNS predictions.

Table 14 Comparison of flexural stress for square-shaped lattice structures considering $\epsilon_{\rm f}=1.8\%$ ($u_0=6.0$ mm).

Unit cell	σ_{f} (MPa)	Differences	
	Experimental (1)	DNS model (2)	(2) to (1)
Size 1	17.32	18.06	4.32%
Size 2	14.59	13.55	7.08%
Size 3	11.39	12.54	10.04%
Size 4	_	12.17	_

the approaches explored in this study. For the visualisation of numerical results, colour maps with displacement magnitude and effective Cauchy stress for triangular-shaped lattice beams with size 3 are shown in Figs. 33 and 34, respectively.

In addition, taking into account the size effect investigation for square-shaped lattice beams, a comparative analysis between computational modelling approaches (multi-scale models and DNS models) and experimental data is presented in Fig. 35. Numerical values and relative differences (in modulus) between the approaches are detailed in Tables 17 and 18, respectively. Colour maps with displacement magnitude and effective Cauchy stress for square-shaped lattice beams with size 3 are shown in Figs. 36 and 37, respectively.

Second-order multi-scale models capture the size effect, whereas first-order multi-scale models exhibit the same response regardless of the UC size. Furthermore, it is worth highlighting that second-order multi-scale models (periodic and minimal) converge towards their corresponding first-order multi-scale models (periodic and uniform traction) for smaller UC sizes.

Table 15 Comparison of the flexural stress (σ_f) associated with UC size for triangular-shaped lattice beams considering $\varepsilon_f = 1.8\%$ ($u_0 = 6.0$ mm).

Analysis type	$\sigma_{ m f}$ (MPa)						
	Size 1	Size 2	Size 3	Size 4	Size 5	Size 6	
Experimental	19.95	14.65	13.05	-	-	_	
DNS model	20.66	14.23	12.95	12.49	_	_	
First-order - Periodic (Per.)	12.06	12.06	12.06	12.06	12.06	12.06	
First-order - Uniform traction (Trac.)	10.11	10.11	10.11	10.11	10.11	10.11	
Second-order - Periodic (Per.)	32.04	17.40	14.49	13.45	12.70	12.43	
Second-order - Minimal (Min.)	31.08	16.77	13.90	12.87	12.13	11.87	

Table 16 Relative differences (in modulus) between multi-scale results, experimental data, and DNS responses for triangular-shaped lattice beams considering $\varepsilon_f = 1.8\%$ ($u_0 = 6.0$ mm).

Case	Differences compared to experimental			Differences compared to DNS				
	First-order		Second-order		First-order		Second-order	
	Per.	Trac.	Per.	Min.	Per.	Trac.	Per.	Min.
Size 1	39.59%	49.36%	60.57%	55.73%	41.66%	51.09%	55.06%	50.39%
Size 2	17.72%	31.02%	18.79%	14.45%	15.31%	29.01%	22.26%	17.80%
Size 3	7.63%	22.57%	11.02%	6.50%	6.93%	21.98%	11.86%	7.31%
Size 4	-	-	-	_	3.51%	19.12%	7.64%	3.04%
Size 5	_	_	_	_	_	_	_	_
Size 6	-	-	-	_	-	-	_	-

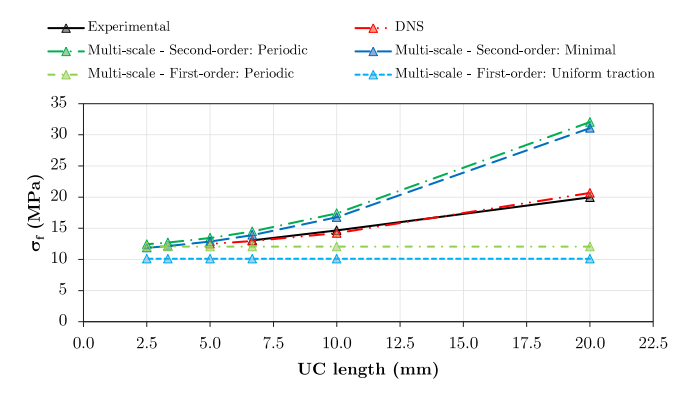


Fig. 32. Size effect study (σ_f versus UC length) for triangular-shaped architected structures considering $\varepsilon_f = 1.8\%$ ($u_0 = 6.0$ mm): comparison of experimental data and DNS results with multi-scale numerical simulation outcomes. (For interpretation of the references to colour in this figure legend, the reader is referred to the web version of this article.)

The UC morphology played an important role in the comparisons between the multi-scale models. For triangular-shaped lattice beams, second-order multi-scale models (periodic and minimal) yield similar results. The same conclusion is observed for the first-order multi-scale models (periodic and uniform traction). In fact, Fig. 34 indicates a similar distribution of effective Cauchy stresses between the deformed UCs associated with the different multi-scale models. The UC with triangular-shaped contains a significant portion of voids on its external surface, where the boundary conditions are defined. Consequently, the reduced amount of solid material on the UC outer boundary smoothes the influence of the boundary condition over the effective mechanical behaviour. On the other hand, significant differences are observed between the second-order multi-scale models as well as between the first-order multi-scale models for square-shaped lattice beams. This can be attributed to the substantial portion of the UC outer boundary being composed of solid material, which increases sensitivity of the results regarding the boundary conditions. Furthermore, the differences in the distribution of the effective Cauchy stresses for the deformed UCs (see Fig. 37) help explain the discrepancy between the multi-scale models.

Larger UC lengths result in significant differences between the experimental data and the multi-scale outcomes. For size 1 ($l_{\mu}=20.00$ mm), the second-order models overestimate the flexural stress,

whereas the first-order models underestimate it. This occurs because the UC length (l_u) is not sufficiently smaller than the macro-scale characteristic length (L), thereby violating the Principle of Scale Separation. In general, multi-scale models tend to provide results more consistent with experimental data for smaller UC sizes (size 2 and size 3), indicating that the Principle of Scale Separation is better established for the architected structure. Specifically, the numerical predictions from the second-order minimal multi-scale model are in close agreement with experimental results for triangular-shaped lattice beams. Although the size effect was not captured, the first-order periodic multi-scale model also provided good results. With regard to square-shaped lattice beams, the numerical results from periodic models (first- and secondorder) demonstrate better agreement with the experimental data. The curvature direction and smoothness in the numerical responses also suggests that the anisotropy induced by 3D printing influenced the experimental data, where possibly the response for size 3 was excessively flexible. In addition, the minimum constraint model (second-order) and the uniform traction model (first-order) proved to be excessively flexible, failing to yield satisfactory results. Despite the lattice material displaying a size effect, the second-order approach did not show substantial advantages. This suggests that the second-order approach can be more suitable for architected materials exhibiting a pronounced size effect, such as structures with smaller thicknesses. For instance, dos Santos et al. (2024) highlights the significant advantages of the secondorder multi-scale approach over the first-order multi-scale strategy for analysing size effects in thin-walled structures.

The multi-scale strategies provided satisfactory results compared to DNS models for coupled architected structures that adhere to the Principle of Scale Separation. In this context, the numerical results from second-order minimal and first-order periodic multi-scale models are in close agreement with DNS predictions for triangular-shaped lattice beams. Moreover, this similarity in results is linked to the distribution of effective Cauchy stresses for the deformed UCs in the multi-scale models and the unit cell results from the DNS model (see Fig. 34). Concerning square-shaped lattice beams, the numerical results from the periodic multi-scale models (particularly for the first-order approach) were more aligned with the DNS responses for smaller UC sizes. In this case, the distribution of effective Cauchy stresses in the deformed configuration of the multi-scale periodic UCs shows good agreement with the unit cell results from the DNS model (see Fig. 37).

Finally, it is worth noting that the DNS models were restricted to a size 4 due to computer memory limitations. This emphasises a drawback of DNS models, which may require an excessive number of

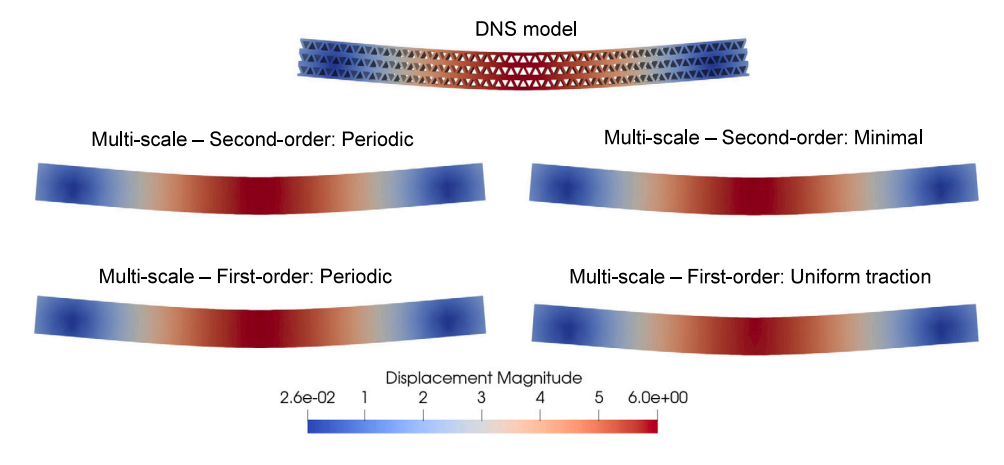


Fig. 33. Displacement magnitude (mm) for different computational modelling options for triangular-shaped lattice beams with size 3 considering $\epsilon_f = 1.8\%$ ($u_0 = 6.0$ mm).

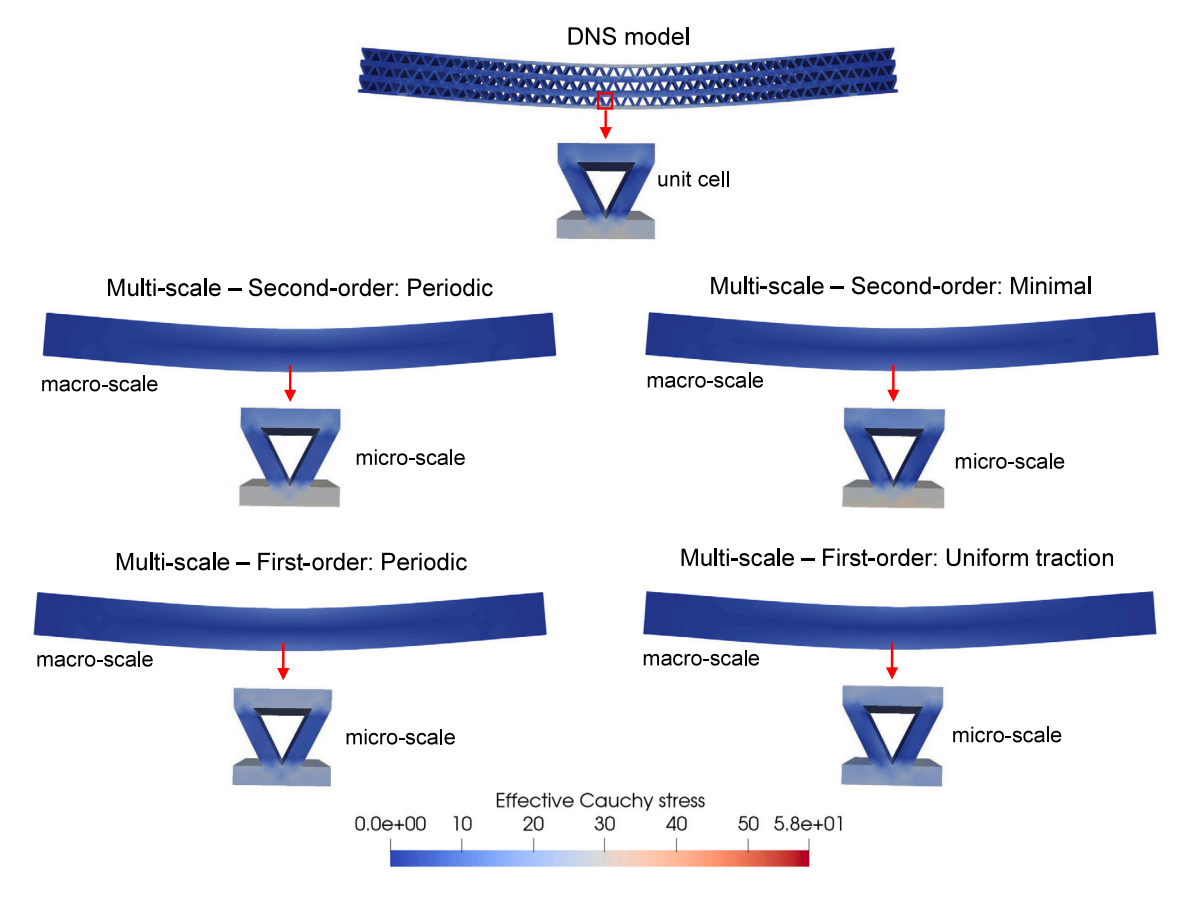


Fig. 34. Effective Cauchy stress (MPa) for different computational modelling options for triangular-shaped lattice beams with size 3 considering $\varepsilon_{\rm f}=1.8\%$ ($u_0=6.0$ mm).

finite elements to discretise all the unit cells in full-scale models. Unlike DNS models, UC sizes 5 and 6 were investigated exclusively using multi-scale approaches. Since the macro and micro meshes remain the same in multi-scale simulations, the computational cost of multi-scale models does not increase significantly for smaller UC sizes. Therefore, multi-scale strategies may offer advantages compared to infeasible DNS models due to their high computational cost.

5. Conclusions

Size effects have been investigated in the mechanical behaviour of additively manufactured architected structures under bending through experimentation and computational modelling approaches, encompassing DNS finite element models and FE² multi-scale simulations based

on first- and second-order homogenisation derived from the variational framework recently proposed by dos Santos et al. (2023). Lattice beams with different unit cell morphologies and the same solid volume fraction were fabricated using the FDM additive manufacturing technique with a commercially available PETG filament. In this context, the present study addressed aspects related to the three-point bending of distinct lattice morphologies, more affordable 3D printing manufacturing, the comparison of advanced modelling strategies, and the evaluation of different micro-scale boundary conditions imposed on the UC in multi-scale analyses.

Material characterisation tests were conducted based on dumbbellshaped specimens, allowing the determination of the elastic constitutive properties of the thermoplastic polymer. Regarding the three-point bending experiments, the good reproducibility of the 3D-printed lattice

Table 17 Comparison of flexural stress (σ_f) associated with UC size for square-shaped lattice beams considering $\varepsilon_f = 1.8\%$ ($u_0 = 6.0$ mm).

Analysis type	$\sigma_{ m f}$ (MPa)						
	Size 1	Size 2	Size 3	Size 4	Size 5	Size 6	
Experimental	17.32	14.59	11.39	_	-	_	
DNS model	18.06	13.55	12.54	12.17	-	-	
First-order - Periodic (Per.)	11.79	11.79	11.79	11.79	11.79	11.79	
First-order - Uniform traction (Trac.)	4.59	4.59	4.59	4.59	4.59	4.59	
Second-order - Periodic (Per.)	30.65	16.99	14.18	13.16	12.41	12.15	
Second-order - Minimal (Min)	22.45	9.79	7.01	5.98	5.22	4.95	

Table 18 Relative differences (in modulus) between multi-scale results, experimental data, and DNS responses for square-shaped lattice beams considering $\epsilon_f = 1.8\%$ ($u_0 = 6.0$ mm).

Case	Differences compared to experimental			Differences compared to DNS				
	First-order		Second-order		First-order		Second-order	
	Per.	Trac.	Per.	Min.	Per.	Trac.	Per.	Min.
Size 1	31.92%	73.51%	76.99%	29.67%	34.74%	74.61%	69.66%	24.30%
Size 2	19.19%	68.55%	16.47%	32.86%	13.03%	66.16%	25.35%	27.74%
Size 3	3.46%	59.74%	24.43%	38.51%	5.98%	63.42%	13.08%	44.12%
Size 4	-	-	-	_	3.11%	62.30%	8.15%	50.89%
Size 5	_	_	_	_	_	_	_	_
Size 6	-	-	-	_	-	-	-	_

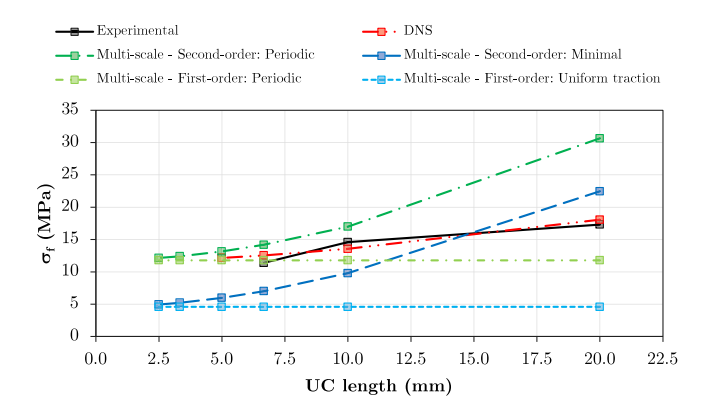


Fig. 35. Size effect study (σ_f versus UC length) for square-shaped architected structures considering $\epsilon_f=1.8\%$ ($u_0=6.0$ mm): comparison of experimental data and DNS results with multi-scale numerical simulation outcomes. (For interpretation of the references to colour in this figure legend, the reader is referred to the web version of this article.)

beams was confirmed by low coefficient of variation values relative to the experimental data on the mechanical behaviour of the tested architected structures. In general, a mechanical behaviour with approximately elastic response was observed before the failure of the beams under bending. Three-point bending tests revealed the size effects on the mechanical behaviour of lattice beams, where a decrease in unit cell size leads to a reduction of the flexural stress in the architected structures. Regarding the size effect study, the lattice beam with triangular-shaped unit cells showed an approximately linear relationship between the unit cell size and the flexural stress, whereas the lattice beam with square-shaped unit cells exhibited a nonlinear behaviour.

DNS predictions showed good agreement with experimental data. Nevertheless, DNS models became unfeasible for lattice beams composed of unit cells with smaller sizes due to the memory limitations of the computer used for performing the numerical simulations. Since a significant number of finite elements are required to obtain the numerical results, full-scale models of architected structures with more refined unit cell arrangements were computationally expensive.

Overall, the main conclusions of the FE² multi-scale simulations for modelling the lattice beams under bending can be summarised as follows:

- UC-based multi-scale models: The numerical results for the
 investigated lattice beam morphologies indicate a sensitivity of
 the micro-scale constraints with respect to the solid material
 portion at the outer boundary of the UC. The results suggest a
 larger gap between the predictions of periodic and minimal multiscale models for the UC with a higher proportion of solid material
 on the outer boundary, and a smaller gap for the UC with a higher
 proportion of voids on the outer surface. This conclusion was
 observed in both the second-order and first-order approaches.
- Size effect: Second-order multi-scale models capture the size effect in lattice beams, with numerical results converging to the corresponding first-order multi-scale models as the UC sizes decrease. Despite capturing the size effect, the second-order multi-scale approach cannot offer significant advantages compared to the classical first-order multi-scale approach. In general, the second-order strategy tends to over-estimate the effective mechanical behaviour of the architected material for larger UC sizes. This aspect, combined with thicker lattice beams, can result in stiffer responses when compared to experimental data. On the other hand, second-order framework explored in this work can offer significant advantages for modelling thin-walled architected materials.
- Applicability: In summary, the Principle of Scale Separation is a key factor to provide satisfactory results when applying multi-scale approaches. In general, the multi-scale numerical results converge to the experimental data and DNS predictions for smaller UC sizes, where the Principle of Scale Separation is better established for the lattice beams under bending. Multi-scale strategies enabled the evaluation of smaller UC sizes without a significant increase in computational cost, offering an advantage over the DNS models that were limited by lack of memory requirements of the processing computer used in the numerical simulations. Furthermore, multi-scale approaches can be a valid modelling option compared to expensive or even unfeasible laboratory experiments, particularly for micro-architected materials that are challenging in terms of manufacturing process.

Finally, the numerical results and experimental data show that the combination of additive manufacturing experiments and numerical modelling strategies discussed here represent a path towards the development of innovative micro-architected structures. The advantages of each approach can be combined for the design of advanced engineering structures, expanding the range of applicability of architected materials.

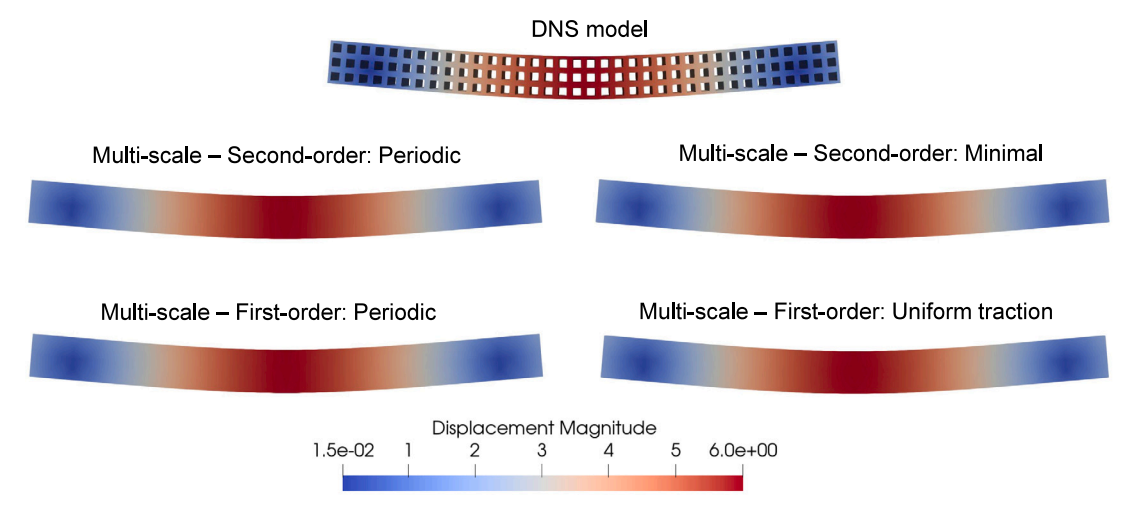


Fig. 36. Displacement magnitude (mm) for different computational modelling options for square-shaped lattice beams with size 3 considering $\epsilon_f = 1.8\%$ ($u_0 = 6.0$ mm).

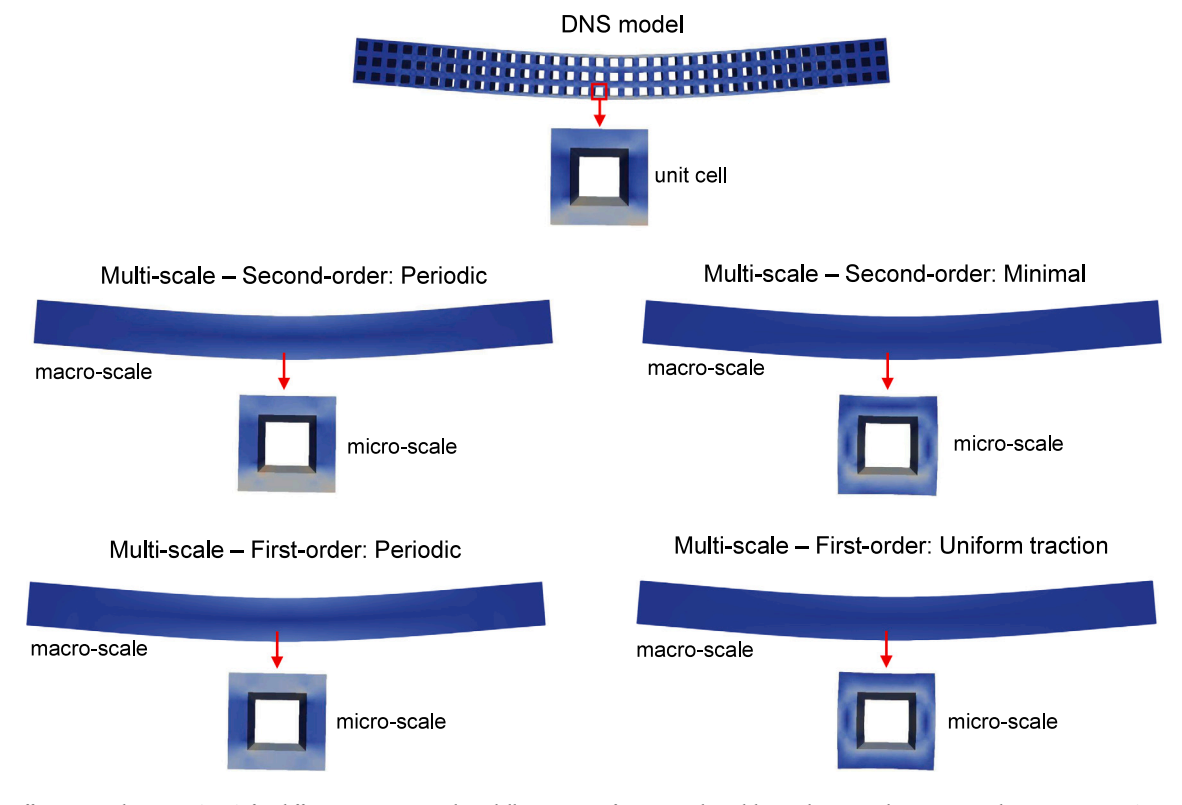


Fig. 37. Effective Cauchy stress (MPa) for different computational modelling options for square-shaped lattice beams with size 3 considering $\epsilon_{\rm f}=1.8\%$ ($u_0=6.0$ mm).

CRediT authorship contribution statement

Wanderson F. dos Santos: Writing – original draft, Visualization, Software, Methodology, Investigation, Data curation, Conceptualization. Alina S.L. Rodrigues: Methodology, Investigation, Formal analysis. Igor A. Rodrigues Lopes: Writing – review & editing, Supervision, Software, Methodology, Conceptualization. Francisco M. Andrade Pires: Writing – review & editing, Supervision, Resources. Sergio P.B. Proença: Writing – review & editing, Supervision, Funding acquisition. Zilda C. Silveira: Writing – review & editing, Supervision, Resources, Methodology.

Declaration of Generative AI and AI-assisted technologies in the writing process

During the preparation of this work the authors used ChatGPT in order to polish the English language quality. After using this tool, the authors reviewed and edited the content as needed and take full responsibility for the content of the published article.

Declaration of competing interest

The authors declare that they have no known competing financial interests or personal relationships that could have appeared to influence the work reported in this paper.

Acknowledgements

The authors would like to sincerely thank Professor Marcelo Aparecido Chinelatto and Laboratory Technician Ricardo Gomes Pereira for their invaluable support in conducting experimental tests at the Laboratory of Mechanical Tests in Polymers of the Department of Materials Engineering, Sao Carlos School of Engineering, University of Sao Paulo (SMM/EESC/USP). Wanderson F. dos Santos, Alina S.L. Rodrigues, and Zilda C. Silveira gratefully acknowledge the financial support provided by the "Coordenação de Aperfeiçoamento de Pessoal de Nível Superior (CAPES)". Igor A. Rodrigues Lopes and Francisco M. Andrade Pires gratefully acknowledge the "Fundação para a Ciência e a Tecnologia (FCT)" for financial support through the project UIDB/50022/2020 (LAETA Base Funding).

Data availability

Data will be made available on request.

References

- Andersen, M.N., Wang, F., Sigmund, O., 2021. On the competition for ultimately stiff and strong architected materials. Mater. Des. 198, 109356. http://dx.doi.org/10. 1016/j.matdes.2020.109356, URL: https://www.sciencedirect.com/science/article/pii/S0264127520308923.
- Ataollahi, S., 2023. A review on additive manufacturing of lattice structures in tissue engineering. Bioprinting 35, e00304. http://dx.doi.org/10. 1016/j.bprint.2023.e00304, URL: https://www.sciencedirect.com/science/article/pii/S2405886623000477.
- Aziz, A.R., Zhou, J., Thorne, D., Cantwell, W.J., 2021. Geometrical scaling effects in the mechanical properties of 3D-printed body-centered cubic (BCC) lattice structures. Polymers 13 (22), http://dx.doi.org/10.3390/polym13223967, URL: https://www. mdpi.com/2073-4360/13/22/3967.
- Benedetti, M., du Plessis, A., Ritchie, R., Dallago, M., Razavi, N., Berto, F., 2021. Architected cellular materials: A review on their mechanical properties towards fatigue-tolerant design and fabrication. Mater. Sci. Eng.: R: Rep. 144, 100606. http://dx.doi.org/10.1016/j.mser.2021.100606, URL: https://www.sciencedirect.com/science/article/pii/S0927796X21000012.
- Bhat, C., Prajapati, M.J., Kumar, A., Jeng, J.-Y., 2024. Additive manufacturing-enabled advanced design and process strategies for multi-functional lattice structures. Materials 17 (14), http://dx.doi.org/10.3390/ma17143398, URL: https://www.mdpi.com/1996-1944/17/14/3398.
- Blanco, P.J., Sánchez, P.J., de Souza Neto, E.A., Feijóo, R.A., 2016. Variational Foundations and Generalized Unified Theory of RVE-Based Multiscale Models. Arch. Comput. Methods Eng. 23 (2), 191–253. http://dx.doi.org/10.1007/s11831-014-9137-5, URL: http://link.springer.com/10.1007/s11831-014-9137-5.
- Chica, L., Alzate, A., 2019. Cellular concrete review: New trends for application in construction. Constr. Build. Mater. 200, 637–647. http://dx.doi.org/10.1016/ j.conbuildmat.2018.12.136, URL: https://www.sciencedirect.com/science/article/ pii/S0950061818331258.
- Ciallella, A., La Valle, G., Vintache, A., Smaniotto, B., Hild, F., 2023. Deformation mode in 3-point flexure on pantographic block. Int. J. Solids Struct. 265–266, 112129. http://dx.doi.org/10.1016/j.ijsolstr.2023.112129, URL: https://www.sciencedirect. com/science/article/pii/S0020768323000264.
- Cuan-Urquizo, E., Silva, R.G., 2023. Fused filament fabrication of cellular, lattice and porous mechanical metamaterials: a review. Virtual Phys. Prototyp. 18 (1), e2224300. http://dx.doi.org/10.1080/17452759.2023.2224300.
- dell'Isola, F., Seppecher, P., Alibert, J.J., Lekszycki, T., Grygoruk, R., Pawlikowski, M., Steigmann, D., Giorgio, I., Andreaus, U., Turco, E., aszewski, M.G., Rizzi, N., Boutin, C., Eremeyev, V.A., Misra, A., Placidi, L., Barchiesi, E., Greco, L., Cuomo, M., Cazzani, A., Corte, A.D., Battista, A., Scerrato, D., Eremeeva, I.Z., Rahali, Y., Ganghoffer, J.-F., Müller, W., Ganzosch, G., Spagnuolo, M., Pfaff, A., Barcz, K., Hoschke, K., Neggers, J., Hild, F., 2019. Pantographic metamaterials: an example of mathematically driven design and of its technological challenges. Contin. Mech. Thermodyn. 31 (4), 851–884. http://dx.doi.org/10.1007/s00161-018-0689-8.
- dos Santos, W.F., Rodrigues, A.S., Rodrigues Lopes, I.A., Andrade Pires, F.M., Proença, S.P., Silveira, Z.C., 2025. Analysis of a novel 3D-printed mechanical metamaterial with tension-induced undulation: Experimental and numerical investigations. Int. J. Solids Struct. 317, 113402. http://dx.doi.org/10.1016/j.ijsolstr.2025.113402, URL: https://www.sciencedirect.com/science/article/pii/S002076832500188X.

- dos Santos, W.F., Rodrigues Lopes, I.A., Andrade Pires, F.M., Proença, S.P., 2023. Second-order multi-scale modelling of natural and architected materials in the presence of voids: Formulation and numerical implementation. Comput. Methods Appl. Mech. Engrg. 416, 116374. http://dx.doi.org/10.1016/j.cma.2023.116374, URL: https://www.sciencedirect.com/science/article/pii/S004578252300498X.
- dos Santos, W.F., Rodrigues Lopes, I.A., Andrade Pires, F.M., Proença, S.P., 2024. Exploring novel mechanical metamaterials: Unravelling deformation mode coupling and size effects through second-order computational homogenisation. Int. J. Solids Struct. 292, 112724. http://dx.doi.org/10.1016/j.ijsolstr.2024.112724, URL: https://www.sciencedirect.com/science/article/pii/S0020768324000817.
- Ferro, C.G., Varetti, S., De Pasquale, G., Maggiore, P., 2018. Lattice structured impact absorber with embedded anti-icing system for aircraft wings fabricated with additive SLM process. Mater. Today Commun. 15, 185–189. http://dx.doi.org/10.1016/ j.mtcomm.2018.03.007, URL: https://www.sciencedirect.com/science/article/pii/ \$235249281730154X.
- Fleck, N.A., Deshpande, V.S., Ashby, M.F., 2010. Micro-architectured materials: past, present and future. Proc. Math. Phys. Eng. Sci. 466, 2495–2516. http://dx.doi.org/10.2307/25706359.
- Iftekar, S.F., Aabid, A., Amir, A., Baig, M., 2023. Advancements and limitations in 3D printing materials and technologies: A critical review. Polymers 15 (11), https://dx.doi.org/10.3390/polym15112519, URL: https://www.mdpi.com/2073-4360/1511/2519
- Iltchev, A., Marcadon, V., Kruch, S., Forest, S., 2015. Computational homogenisation of periodic cellular materials: Application to structural modelling. Int. J. Mech. Sci. 93, 240–255. http://dx.doi.org/10.1016/j.ijmecsci.2015.02.007, URL: https://www.sciencedirect.com/science/article/pii/S0020740315000612.
- Jiao, P., Raney, J.R., Zheng, X., Alavi, A.H., 2023. Mechanical metamaterials and beyond. Nat. Commun. 14, 6004. http://dx.doi.org/10.1038/s41467-023-41679-8.
- Kladovasilakis, N., Tsongas, K., Karalekas, D., Tzetzis, D., 2022. Architected materials for additive manufacturing: A comprehensive review. Materials 15 (17), http://dx.doi.org/10.3390/ma15175919, URL: https://www.mdpi.com/1996-1944/15/17/5919.
- Kladovasilakis, N., Tsongas, K., Tzetzis, D., 2023. Development of novel additive manufactured hybrid architected materials and investigation of their mechanical behavior. Mech. Mater. 176, 104525. http://dx.doi.org/10.1016/j.mechmat.2022.104525, URL: https://www.sciencedirect.com/science/article/pii/S0167663622002897.
- Korshunova, N., Alaimo, G., Hosseini, S., Carraturo, M., Reali, A., Niiranen, J., Auricchio, F., Rank, E., Kollmannsberger, S., 2021. Bending behavior of octet-truss lattice structures: Modelling options, numerical characterization and experimental validation. Mater. Des. 205, 109693. http://dx.doi.org/10.1016/j.matdes.2021.109693, URL: https://www.sciencedirect.com/science/article/pii/S0264127521002458.
- Li, X., Yu, X., Chua, J.W., Lee, H.P., Ding, J., Zhai, W., 2021. Microlattice metamaterials with simultaneous superior acoustic and mechanical energy absorption. Small 17 (24), 2100336. http://dx.doi.org/10.1002/smll.202100336, URL: https://onlinelibrary.wiley.com/doi/abs/10.1002/smll.202100336.
- Lopes, I.A.R., Ferreira, B.P., Pires, F.M.A., 2021. On the efficient enforcement of uniform traction and mortar periodic boundary conditions in computational homogenisation. Comput. Methods Appl. Mech. Engrg. 384, 113930. http://dx.doi.org/10.1016/j.cma.2021.113930, URL: https://linkinghub.elsevier.com/retrieve/pii/S004578252100267X.
- Mahmoud, D., Elbestawi, M.A., 2017. Lattice structures and functionally graded materials applications in additive manufacturing of orthopedic implants: A review. J. Manuf. Mater. Process. 1 (2), http://dx.doi.org/10.3390/jmmp1020013, URL: https://www.mdpi.com/2504-4494/1/2/13.
- Molavitabrizi, D., Khakalo, S., Bengtsson, R., Mousavi, S.M., 2023. Second-order homogenization of 3-D lattice materials towards strain gradient media: numerical modelling and experimental verification. Contin. Mech. Thermodyn. 35 (6), 2255–2274. http://dx.doi.org/10.1007/s00161-023-01246-4.
- Nazir, A., Abate, K.M., Kumar, A., Jeng, J.-Y., 2019. A state-of-the-art review on types, design, optimization, and additive manufacturing of cellular structures. Int. J. Adv. Manuf. Technol. 104 (9), 3489–3510. http://dx.doi.org/10.1007/s00170-019-04085-3.
- Nguyen, V.-D., Noels, L., 2014. Computational homogenization of cellular materials. Int. J. Solids Struct. 51 (11–12), 2183–2203, URL: http://dx.doi.org/10.1016/j.ijsolstr. 2014.02.029.
- Opgenoord, M.M.J., Willcox, K.E., 2021. Design for additive manufacturing: cellular structures in early-stage aerospace design. Struct. Multidiscip. Optim. 60 (2), 411–428. http://dx.doi.org/10.1007/s00158-019-02305-8.
- Pan, C., Han, Y., Lu, J., 2020. Design and optimization of lattice structures: A review. Appl. Sci. 10 (18), http://dx.doi.org/10.3390/app10186374, URL: https://www.mdpi.com/2076-3417/10/18/6374.
- Pham, R.D., Hütter, G., 2021. Influence of topology and porosity on size effects in stripes of cellular material with honeycomb structure under shear, tension and bending. Mech. Mater. 154, 103727. http://dx.doi.org/10.1016/j.mechmat.2020.103727, URL: https://www.sciencedirect.com/science/article/pii/s0167669690307511
- Plocher, J., Panesar, A., 2019. Review on design and structural optimisation in additive manufacturing: Towards next-generation lightweight structures. Mater. Des. 183, 108164, URL: https://www.sciencedirect.com/science/article/pii/ S0264127519306021 doi:doi.org/10.1016/j.matdes.2019.108164.

- Popł awski, A., Bogusz, P., Grudnik, M., 2025. Digital image correlation and numerical analysis of mechanical behavior in photopolymer resin lattice structures. Materials 18 (2), http://dx.doi.org/10.3390/ma18020384, URL: https://www.mdpi.com/ 1996-1944/18/2/384.
- Qi, C., Jiang, F., Yang, S., 2021. Advanced honeycomb designs for improving mechanical properties: A review. Compos. Part B: Eng. 227, 109393. http://dx.doi.org/10.1016/j.compositesb.2021.109393, URL: https://www.sciencedirect.com/science/article/pii/S1359836821007642.
- Rahali, Y., Giorgio, I., Ganghoffer, J., dell'Isola, F., 2015. Homogenization à la piola produces second gradient continuum models for linear pantographic lattices. Internat. J. Engrg. Sci. 97, 148–172. http://dx.doi.org/10.1016/j.ijengsci.2015.10.003, URL: https://www.sciencedirect.com/science/article/pii/S0020722515001391.
- Rodrigues Lopes, I.A., Andrade Pires, F.M., 2022a. A fully second-order homogenization formulation for the multi-scale modeling of heterogeneous materials. Internat.

 J. Numer. Methods Engrg. 123 (21), 5274–5318. http://dx.doi.org/10.1002/nme. 7063, URL: https://onlinelibrary.wiley.com/doi/abs/10.1002/nme.7063.
- Rodrigues Lopes, I.A., Andrade Pires, F.M., 2022b. Unlocking the potential of secondorder computational homogenisation: An overview of distinct formulations and a guide for their implementation. Arch. Comput. Methods Eng. 29, 1339–1393. http://dx.doi.org/10.1007/s11831-021-09611-9.
- Schaedler, T.A., Carter, W.B., 2016. Architected cellular materials. Annu. Rev. Mater. Res. 46 (Volume 46, 2016), 187–210. http://dx.doi.org/10.1146/annurev-matsci-070115-031624, URL: https://www.annualreviews.org/content/journals/10.1146/annurev-matsci-070115-031624.
- Smeets, B.J., Fagan, E.M., Matthews, K., Telford, R., Murray, B.R., Pavlov, L., Weafer, B., Meier, P., Goggins, J., 2021. Structural testing of a shear web attachment point on a composite lattice cylinder for aerospace applications. Compos. Part B: Eng. 212, 108691. http://dx.doi.org/10.1016/j.compositesb.2021.108691, URL: https://www.sciencedirect.com/science/article/pii/S1359836821000846.
- Spadaccini, C.M., 2019. Additive manufacturing and processing of architected materials. MRS Bull. 44 (10), 782–788. http://dx.doi.org/10.1557/mrs.2019.234.
- Tay, Y.Y., Lim, C.S., Lankarani, H.M., 2014. A finite element analysis of high-energy absorption cellular materials in enhancing passive safety of road vehicles in sideimpact accidents. Int. J. Crashworthiness 19 (3), 288–300. http://dx.doi.org/10. 1080/13588265.2014.893789.
- Tekoglu, C., Onck, P.R., 2005. Size effects in the mechanical behavior of cellular materials. J. Mater. Sci. 40 (22), 5911–5917. http://dx.doi.org/10.1007/s10853-005-5042-5.
- Tilley, R., Holmes, D., Pickering, E., Woodruff, M., 2024. 3D printed metamaterials for energy absorption in motorsport applications. Int. J. Automot. Technol. 25 (6), 1529–1540. http://dx.doi.org/10.1007/s12239-024-00136-1.
- Tiwari, A.K., Pratapa, P.P., Santhanam, M., 2024. Lattice concrete: 3D printed periodic cellular structures through selective cement hydration. J. Build. Eng. 86, 108946. http://dx.doi.org/10.1016/j.jobe.2024.108946, URL: https://www.sciencedirect.com/science/article/pii/S235271022400514X.
- Uribe-Lam, E., Treviño-Quintanilla, C.D., Cuan-Urquizo, E., Olvera-Silva, O., 2021. Use of additive manufacturing for the fabrication of cellular and lattice materials: a review. Mater. Manuf. Process. 36 (3), 257–280. http://dx.doi.org/10.1080/10426914.2020.1819544.
- Wang, E., Yao, R., Li, Q., Hu, X., Sun, G., 2024. Lightweight metallic cellular materials: A systematic review on mechanical characteristics and engineering applications. Int. J. Mech. Sci. 270, 108795. http://dx.doi.org/10.1016/j.ijmecsci.2023.108795, URL: https://www.sciencedirect.com/science/article/pii/S0020740323006975.

- Wang, Y., Zhang, X., Li, Z., Gao, H., Li, X., 2022. Achieving the theoretical limit of strength in shell-based carbon nanolattices. Proc. Natl. Acad. Sci. 119 (34), e2119536119. http://dx.doi.org/10.1073/pnas.2119536119, URL: https://www. pnas.org/doi/abs/10.1073/pnas.2119536119.
- Weeger, O., 2021. Numerical homogenization of second gradient, linear elastic constitutive models for cubic 3D beam-lattice metamaterials. Int. J. Solids Struct. 224, 111037. http://dx.doi.org/10.1016/j.ijsolstr.2021.03.024, URL: https://www.sciencedirect.com/science/article/pii/S0020768321001153.
- Wu, Y., Fang, J., Wu, C., Li, C., Sun, G., Li, Q., 2023a. Additively manufactured materials and structures: A state-of-the-art review on their mechanical characteristics and energy absorption. Int. J. Mech. Sci. 246, 108102. http://dx.doi.org/10.1016/j.ijmecsci.2023.108102, URL: https://www.sciencedirect.com/science/article/pii/S0020740323000048.
- Wu, L., Mustafa, M., Segurado, J., Noels, L., 2023b. Second-order computational homogenisation enhanced with non-uniform body forces for non-linear cellular materials and metamaterials. Comput. Methods Appl. Mech. Engrg. 407, 115931. http://dx.doi.org/10.1016/j.cma.2023.115931, URL: https://www.sciencedirect.com/science/article/pii/S0045782523000543.
- Yang, H., Abali, B.E., Müller, W.H., Barboura, S., Li, J., 2022. Verification of asymptotic homogenization method developed for periodic architected materials in strain gradient continuum. Int. J. Solids Struct. 238, 111386. http://dx.doi.org/10. 1016/j.ijsolstr.2021.111386, URL: https://www.sciencedirect.com/science/article/ pii/S0020768321004510.
- Yang, H., Liu, Z., Xia, Y., Fan, W., Taylor, A.C., Han, X., 2024. Mechanical properties of hierarchical lattice via strain gradient homogenization approach. Compos. Part B: Eng. 271, 111153. http://dx.doi.org/10.1016/j.compositesb.2023.111153, URL: https://www.sciencedirect.com/science/article/pii/S135983682300656X.
- Yang, H., Müller, W.H., 2021. Size effects of mechanical metamaterials: a computational study based on a second-order asymptotic homogenization method. Arch. Appl. Mech. 91, http://dx.doi.org/10.1007/s00419-020-01808-x.
- Yavas, D., Liu, Q., Zhang, Z., Wu, D., 2022. Design and fabrication of architected multi-material lattices with tunable stiffness, strength, and energy absorption. Mater. Des. 217, 110613. http://dx.doi.org/10.1016/j.matdes.2022.110613, URL: https://www.sciencedirect.com/science/article/pii/S0264127522002349.
- Yildizdag, M.E., Barchiesi, E., dell'Isola, F., 2020. Three-point bending test of panto-graphic blocks: numerical and experimental investigation. Math. Mech. Solids 25 (10), 1965–1978. http://dx.doi.org/10.1177/1081286520916911.
- Yin, H., Zhang, W., Zhu, L., Meng, F., Liu, J., Wen, G., 2023. Review on lattice structures for energy absorption properties. Compos. Struct. 304, 116397. http://dx.doi.org/10.1016/j.compstruct.2022.116397, URL: https://www.sciencedirect.com/science/article/pii/S0263822322011291.
- Zhang, J., Liu, Y., Babamiri, B.B., Zhou, Y., Dargusch, M., Hazeli, K., Zhang, M.-X., 2022. Enhancing specific energy absorption of additively manufactured titanium lattice structures through simultaneous manipulation of architecture and constituent material. Addit. Manuf. 55, 102887. http://dx.doi.org/10.1016/j.addma.2022.102887, URL: https://www.sciencedirect.com/science/article/pii/S221486042200286X.